SANDIA REPORT
SAND2019-14443
Unlimited Release
Printed November 2019

Development of Fast-Pulse Neutron Generation Capability by Beam-Target Interaction on HERMES-III for Radiation Effects Testing: Final Report

Timothy J. Renk

Directed Energy Assessments

Paul F. Ottinger

Syntek Technologies, Arlington, VA 22030 USA

Russell E. Durrer

Sigma Science, Inc. Albuquerque, NM 87110

Prepared by
Sandia National Laboratories
Albuquerque, New Mexico 87185 and Livermore, California 94550

Sandia National Laboratories is a multimission laboratory managed and operated by National Technology and Engineering Solutions of Sandia, LLC, a wholly owned subsidiary of Honeywell International, Inc., for the U.S. Department of Energy's National Nuclear Security Administration under contract DE-NA0003525.

Issued by Sandia National Laboratories, operated for the United States Department of Energy by National Technology and Engineering Solutions of Sandia, LLC.

NOTICE: This report was prepared as an account of work sponsored by an agency of the United States Government. Neither the United States Government, nor any agency thereof, nor any of their employees, nor any of their contractors, subcontractors, or their employees, make any warranty, express or implied, or assume any legal liability or responsibility for the accuracy, completeness, or usefulness of any information, apparatus, product, or process disclosed, or represent that its use would not infringe privately owned rights. Reference herein to any specific commercial product, process, or service by trade name, trademark, manufacturer, or otherwise, does not necessarily constitute or imply its endorsement, recommendation, or favoring by the United States Government, any agency thereof, or any of their contractors or subcontractors. The views and opinions expressed herein do not necessarily state or reflect those of the United States Government, any agency thereof, or any of their contractors.

Printed in the United States of America. This report has been reproduced directly from the best available copy.

Available to DOE and DOE contractors from
U.S. Department of Energy
Office of Scientific and Technical Information
P.O. Box 62
Oak Ridge, TN 37831

Telephone: (865) 576-8401
Facsimile: (865) 576-5728
E-Mail: reports@osti.gov
Online ordering: http://www.osti.gov/scitech

Available to the public from
U.S. Department of Commerce
National Technical Information Service
5301 Shawnee Rd
Alexandria, VA 22312

Telephone: (800) 553-6847
Facsimile: (703) 605-6900
E-Mail: orders@ntis.gov
Online order: https://classic.ntis.gov/help/order-methods/

SAND2019-14443
Printed November 2019
Unlimited Release

Development of Fast-Pulse Neutron Generation Capability by Beam-Target Interaction on HERMES-III for Radiation Effects Testing: Final Report

Timothy J. Renk

Directed Energy Assessments

Paul F. Ottinger

Syntek Technologies, Arlington, VA 22030 USA

Russell E. Durrer

Sigma Science, Inc. Albuquerque, NM 87110

Abstract

The goal of this Project is to produce an intense neutron pulse on HERMES III using the beam-target method with an intense proton beam. The potential advantage of proton use is that the generated neutron spectrum contains significantly more high-energy neutrons than that produced by electron-beam generated photoneutrons using the same facility. And compared to (D,T) facilities such as NIF, no tritium (or deuterium) is required for this process. To achieve the ~ mid 10^{10} neutrons/cm^2 at a test object location listed as the goal in the Proposal, it was proposed that a radial ion diode previously developed and fielded at the 6 MeV - level be extended in performance to the full-power level on HERMES, with proton energies in the neighborhood of 15 MeV. This Report details the successful development of the radial ion diode at full power, which required more durable hardware which could be fielded at a one shot/day basis with minimal debris and activation (an important concern), and which could be substituted quickly into the normal negative-polarity bremsstrahlung source experiments without compromising the main HERMES validation mission. As direct measurement of proton beam characteristics proved challenging, the Project relied on an extensive series of simulations, LSP for beam dynamics and MCNP to characterize neutron output. Simulation results will be discussed, including the conclusion that neutron measurements made are consistent with an MCNP-predicted proton beam of 16 MeV peak energy, and 200 kA peak current. This Project also contributes to physics understanding of the use of inductive voltage adder (IVA) platforms to drive diode loads. Since such diodes operate independently of the physics of IVAs, the IVA-diode coupling requires matching of the MITL flow to the requirements of ion diode operation.

ACKNOWLEDGMENTS

The authors acknowledge fruitful conversations concerning this Report with Dr. Bryan V. Oliver, the Project Manager for this LDRD Project. The authors also acknowledge the important work by the HERMES crew in supporting these experiments at the HERMES-III facility: Gary Tilley, Ben Hughes, Keith Tunell, and Mo Archuletta.

TABLE OF CONTENTS

1. Executive Summary……..……9

2. Introduction……...11

3. Use of beam-target interaction to yield neutrons..……14

4. Radial diode development at half-machine power (2008 - 2010) ..……16

5. Radial diode development at full-machine (2017 – 2019) ……20
   5.1. LSP simulations of the radial ion diode……...20

6. Characterization of ion beam properties using Faraday cups, Rogowski coils, and calorimeter……..……25

   6.1 Shadowbox/witness plate technique……...26
   6.2 Faraday cups……..27
   6.3 Rogowski coil to measure total ion current……...28
   6.4 Calorimeter for measuring heat deposited by the ion beam…….28

7. Debris Mitigation……..……..…30

8. MCNP simulations to predict neutron fluence and spectrum…….....36

   8.1 MCNP predictions of neutron flux uniformity in the test fixture..41

9. Dosimetry measurements compared to MCNP predictions……42

10. Conclusions and suggestions for future work……46

11. References……47

FIGURES

Figure 1.a. Neutron yield vs proton energy for Ta181(p,2n)W180 reaction.
b. Neutron yield vs proton energy for Ta181(p,n)W181 reaction. ……..15

Figure 2. conceptual drawing of axial ion diode connected to an IVA ……..……16

Figure 3. Conceptual drawing of HERMES electron flow in negative polarity (top) vs positive polarity (bottom)……..……18

Figure 4. Photograph of shadowbox/witness plate assembly after an initial axial diode experiment at half-machine power……...……19

Figure 5. Conceptual drawing of radial ion diode as designed for HERMES…..……..20

Figure 6. particle flow from LSP simulation at full-machine power for MITL electrons (left), diode electrons (center), and ions in forward direction (right)..……...21

Figure 7.a. Total and bound currents at z = -2 meters, ion diode and bremsstrahlung shots compared. **b.** MITL impedance at z = -2 meters, ion diode and bremsstrahlung shots compared…..……22

Figure 8. LSP currents at z = -2 meters chosen to match experimental currents: I_A, I_C, and electron flow current……..……...24

Figure 9.a. LSP predictions for currents near A-K gap: I_A, I_C, and electron flow current.
b. LSP predictions for voltage at various z-locations ……..25

Figure 10.a. Front surface, shadowbox aperture plate, after a shot. **b**. Back of aperture plate after same shot.……..27

Figure 11. Shadowbox witness plate after same shot as in Fig. 10. ……27

Figure 12. Faraday cup, Rogowski coil, and (scaled) voltage waveforms from several shots…….……28

Figure 13.a. Calorimeter front plate, pre-shot. **b**. Calorimeter waveforms from a shot...29

Figure 14. Calorimeter front plate, after 2 shots. Closeup on right……..30

Figure 15. Damage to aperture plate front and witness plate after a half-machine shot, shot 8893 (previous Project)..……..…31

Figure 16.a. Radial diode anode tube, initial shot (2017) using aluminum. **b.** Anode tube, steel, shot in June 2019……...31

Figure 17. Conceptual 3-dimensional assembly drawing, radial diode, showing front and rear beam diagnostic hardware…...……..33

Figure 18. Conceptual drawing side view, front test fixture ……..……..33

Figure 19. Photographs, front (a) and rear (b) test fixture covers, after a June 2019 shot… ……..…….34

Figure 20. Photograph, front test fixture cover with neutron target, post-shot…….35

Figure 21.a. Assembly drawing, replacement rear beam stop. B**.** Photograph of fabricated beam stop……..……..36

Figure 22. Schematic drawing, top view, of HERMES high-bay and Test Cell. ……...37

Figure 23. Predicted neutron output into 4π compared for three sources, all neutrons (a), all neutrons > 1 MeV energy (b), and all neutrons > 5 MeV energy (c) ……38

Figure 24. Predicted total neutron output into forward cone, three sources, plotted semi-log (a) and linear (b). ……..…..39

Figure 25. Predicted neutron output, three sources (semi-log), plotted with measured neutron spectrum from Sanford paper (1993)…….…...39

Figure 26. Predicted neutron spectrum (normalized), ion diode compared to ACRR, for energies 0 -15 MeV (a) and 0 – 0.3 MeV (b)…….….40

Figure 27. Predicted neutron spectrum (normalized), ion diode compared to Cf252 source, for energies 0 -14 MeV (a) and 0 – 0.2 MeV (b)…….…….41

Figure 28.a. Front of test fixture divided into 1 cm rings for display of neutron flux prediction from MCNP. **b.** Predicted neutron flux behind front fixture plate as function of radius……42

EXECUTIVE SUMMARY of Project 200267

1. The HERMES ion diode neutron source LDRD appears to have achieved its key goal of ~ few 10^{10} pulsed neutrons/cm^2 at a test object location. Further neutron measurements are needed to confirm this.

2. The HERMES radial ion diode operation, previously developed at half-power (6 MeV), was successfully extended to an estimated 16 MeV (peak) and 200 kA proton current, thus making this ion beam the most powerful in the world in current operation. At Sandia, such energetic ions have not been produced since the PFBA-II experiments. MCNP and LSP simulations were key to understanding diode performance and predicting neutron output and spectrum.

3. Despite this power, the contents of the test fixture, located as close as 1.25 cm to the neutron source, are undamaged after multiple ion beam pulses.

4. Results show that beam/target interaction, used on a > 10 MeV platform, can yield a pulsed neutron flux that is competitive with photoneutrons and dense plasma focus (DPF) as a neutron source.

5. The radial ion diode is operationally successful, being operated with minimal debris and activation, and could be inserted readily into the normal bremsstrahlung operation, thus minimally impacting the HERMES main validation mission.

NOMENCLATURE

Abbreviation	Definition
IVA	Inductive Voltage Adder
MITL	Magnetically insulated transmission line
TLD	Thermoluminescent dosimeter
LSP	Particle-in-cell code, software product of ATK Mission Research, Albuquerque, NM.
MCNP	Monte Carlo N-Particle Transport Code, software package developed by Los Alamos National Laboratory

2. INTRODUCTION

There is an ongoing need for a source of pulsed neutrons of sufficient flux and energy for effects testing. By pulsed is meant a timescale ~ tens or hundreds of nanoseconds. A rough indicator of sufficient flux would be a concentration exceeding 1 x 10^{10} neutrons/cm^2 over some volume at the test object location. This flux level lies beyond what neutron sources such as portable neutron generators can produce. Existing intense neutron sources such as the National Ignition Facility (NIF) at Lawrence Livermore National Laboratory (LLNL) [1] and the OMEGA laser facility at the University of Rochester [2] produce fluences significantly exceeding the threshold level mentioned. They rely on the deuterium-tritium (D-T) fusion reaction to produce copious amounts of 14 MeV neutrons. There are also neutron sources based upon the dense plasma focus (DPF) process [3], which generally operate with either (D-T) or (D-D) fusion reactions. The latter produces neutrons of approximately 2.45 MeV energy.

Another method of pulsed neutron production involves the use of intense particle beams which impinge upon solid targets. This method is known as 'beam-target'. The source of the beam can be either electrons or ions. In the case of electrons, intense electron beams impinge upon a high-atomic-weight metal such as tantalum, leading to a burst of photons by the bremsstrahlung process. The photons so generated interact with the tantalum, resulting in the production of neutrons [4]. These photon-produced neutrons are referred to as *photoneutrons*. Data presented in [4] indicate a threshold of photoneutron production in a tantalum target of approximately 10 MeV electron energy. The HERMES III facility has been previously investigated as a source of photoneutrons [5], with neutron flux and spectrum characterized through extensive use of neutron dosimetry.

High-energy ions can also be used to produce neutrons, through (p,*x*n) reactions, where *x* can be unity or greater. There exist any number of elements [6], mostly metals, in which such (p,*x*n) reactions have high cross-sections approaching 1 barn (peak). In general, protons are the most easily-produced impinging ion species, and proton energies greater than 10 MeV are required to obtain useful neutron yields. Heavier ions need significantly higher energies than 10 MeV, since for the same accelerating voltage, their attained velocities are much lower.

In both cases of electron and ion-generated neutron flux by beam-target, the neutrons produced do not have single or near-single energies, as with (D-D) and (D-T), but result in a *spectrum* of energies. Accordingly, it is important to characterize not only the total neutron flux produced, but the neutron spectrum, which as it turns out, is very different between the electron-produced photoneutrons, and neutrons produced by proton impingement. Experimental neutron spectrum characterization requires the fielding of an extensive array of neutron dosimetry samples, but can also be estimated using the MCNP simulation code [7,8]. We report here the result of MCNP simulations of both proton-generated neutron spectra and photoneutron spectra, both produced in experiments on the HERMES III facility.

Since producing neutrons efficiently using either electron and ion-induced neutron processes as described above require accelerating voltages greater than 10 MV, HERMES III is an appropriate platform for generation of beam-target neutrons. As already mentioned, it has already been in use as a source of bremsstrahlung photons (and therefore photoneutrons). It will be shown in this Report that one advantage of proton-induced neutrons over photoneutrons produced by HERMES is that the spectrum generated by protons has a higher proportion of high-energy neutrons.

Any plan to implement an ion diode on HERMES needs to address both physics- and operational-based issues. Among the physics questions is: what kind of ion diode should be used? This is not a trivial question. Almost all intense ion beam sources such as those operated on the prior Proto-I [9] and PBFA-II [10,11] machines operated at Sandia have been connected to a high-voltage interface. That is, a forward-going voltage pulse crosses from a water to vacuum section through a barrier that can withstand the voltage transferred without suffering a voltage breakdown. In particular, a high-voltage interface does not

produce a forward-going electron flow, such as that which occurs in the HERMES inductive voltage adder (IVA) driver which is attached to a magnetically insulated transmission line (MITL). The forward-going voltage pulse is transferred to an ion diode that operates independently of the generator. In the case of both Proto-I and PBFA-II, the diode type was a magnetically insulated ion diode [9]. Such a diode contains external field coils that suppress electron generation, in order to impart the maximum amount of energy to the resultant ion beam. Combined with an advanced ion source such as that operated on the RHEPP-1 facility, also located at Sandia [12], such diodes can result in an ion efficiency (ion current compared to total current generated) of as high as 70%.

When the driver is an IVA, however, a significant portion of the current coming forward consists of electron flow, as opposed to current flowing within the outer and inner MITL conductors. In a MITL, the applied electric field at the cathode exceeds the threshold for electron emission. The emitted electron flow, behind an initial loss front, becomes magnetically insulated as the rising current bends the electrons back towards the cathode. The amount of electron flow is determined by the vacuum MITL impedance. In HERMES, the vacuum impedance is a relatively low 34 ohms, which results in two-thirds of the current coming forward in electron flow when run with a load at the self-limited impedance. The presence of external field coils such as in a magnetically insulated ion diode would likely disrupt the forward-going electron flow, leading to the loss of flow current before it would reach the diode itself. The loss of two-thirds of the generator current would in turn likely restrict the ion efficiency of the ion diode. An alternative diode type is a self-field ion diode [13,14], in which the diode electron flow is suppressed by fields within the diode itself, as opposed to fields imposed from external coils. Such a diode was operated on HERMES at half-machine power in a previous LDRD project [13,14]. The ion efficiency of such self-field diodes is lower than for magnetically insulated diodes. Since the ion efficiency is a fraction of the total diode current, it is important that the electron flow into the diode region not be disrupted, but in fact contributes maximally to the currents within the diode itself. This Report details the development of the design of the self-field diode operated on HERMES at full machine power, at somewhat less than the self-limited impedance, but still high enough impedance to maintain high voltage above 10 MV. Initial diode development took place within the prior LDRD project [13,14], resulting in what is known as a radial ion diode. The LSP code [15] was instrumental in the design and operation of the radial ion diode, which relies on magnetic insulation to maintain both diode impedance throughout the power pulse, and minimize damage to diode hardware. Attempts to characterize the resultant ion beam using conventional ion diagnostics such as Faraday cups, Rogowski coils and calorimeters is discussed. Such attempts proved challenging, and ultimately were superseded by the placement of dosimeter foils placed within test fixtures to measure neutron flux directly. Characterization of neutrons was concentrated heavily on MCNP simulations, as will be discussed.

In addition to the physics of the generation and characterization of the ions and neutron fluxes, there are considerable operational considerations for successful implementation of ion beam operation on HERMES. The dominant HERMES mission requires operation in negative polarity, which requires that any ion beam operated on HERMES at full power must propagate *into* the machine. While expected applications are not affected by this, the preferred direction for beam extraction would be outside the machine, which would allow for convenient fielding of ion beam diagnostics. Negative polarity operation restricts the choice of diagnostics that can be fielded to characterize the ion beam. This restricted area, plus budgetary restrictions, limited the diagnostics suite to the rather simple set already mentioned above.

The dominant HERMES qualification mission requires almost constant operation of the bremsstrahlung diode mode. Therefore, any ion diode experiments must satisfy the following operational requirements: 1) changes to the diode region to accommodate ion diode hardware must be made quickly, at both setup and takedown times; 2) debris must be kept as low as possible, so as to not compromise subsequent bremsstrahlung experiments; and 3) any activation occurring as a result of high-energy protons impinging on targets for neutron generation must be minimized, both to attain a one shot/day operation of the ion

diode, and to minimize down time for the switchover back to bremsstrahlung operation. These requirements have been addressed and satisfied, and details will be discussed in this Report.

The remainder of this Report is divided into the following sections:

1) **Use of beam-target interaction to yield neutrons.** Protons impinging upon metal foil targets can access (p,*x*n) reactions (where *x* is an integer ≥ 1) that result in neutron generation. The (p,*x*n) abbreviation refers to a process whereby a high-energy (generally > 10 MeV) proton impinges on a nucleus, resulting in one or more neutrons escaping the nucleus. Cross-sections for such reactions have a roughly Gaussian profile characterized by a peak cross-section value (in barns), the proton energy at which the peak cross-section occurs, and an energy threshold for the reaction. The goal is to maximize neutron yield while minimizing the production of activation caused by transmutation creating radioactive daughter products which have undesirably long half-lives.

2) **A brief review of the diode development experiments at HERMES half-power in a previous LDRD Project (Project 117680, 2008-10),** which culminated in the radial diode design. This work was later published [14], and LSP simulations described at half-power are also relevant for (and discussed) at full-power (below). Accordingly, the simulation results will be discussed as part of the full-power results.

3) **Description of the geometry of the diode region, including schematic geometry for LSP simulations. Simulations results are discussed,** and compared to waveforms from HERMES ion diode shots for comparison. This includes diode impedance, voltage, and proton current. Simulations predict the presence of two ion beams, one propagating into the machine, and a "backward" ion beam, which is described further.

4) **Characterization of beam properties using diagnostics previously mentioned (Faraday cups, Rogowski coils, calorimeter).** The diode environment is challenging for such diagnostics, since they must operate while the high-energy beam is impinging upon them. Only approximate values of current density and total current were determined.

5) **Debris mitigation.** Besides minimal activation as an experiment goal, it is important to limit debris caused by ion beam operation. Use of the standard bremsstrahlung diode generates little or no debris. If the ion beam experiments produced extra debris not seen in bremsstrahlung experiments, this could be expected to delay resumption of standard shots after a campaign of ion diode shots is concluded. The seriousness of the delay could depend upon where the debris is located post-shot. Debris located near the diode region can be removed relatively easily. Debris projected a significant distance in the MITL towards the cavity assemblies can be hard to remove, and could adversely affect subsequent HERMES operation. The activation question is addressed in the next discussion section. Debris mitigation continues throughout the course of the Project, and was resolved satisfactorily only towards the Project end, as will be discussed.

6) **MCNP simulations are performed** to predict a) neutron spectrum at the test object position, and b) neutron flux in number/cm^2 at the same location. Input voltage and current is provided by both experimental data, and by LSP estimates. The concept of multiple sub-range neutron foils to enhance neutron dose is discussed. Several sets of pairs of metal foils (fractions of mm-thickness each) were investigated in HERMES investigations, including foils of cobalt, zirconium, niobium, and tantalum. Predicted neutron spectra are compared using the following targets: a) dual foil cobalt-niobium, b) thick target tantalum, and c) photoneutron spectrum produced by the standard mode HERMES bremsstrahlung diode operated at full-power with a 53 cm anode-cathode (A-K) gap. The normalized

ion diode-produced neutron spectral shape is compared to that produced by the Annular Core Research Reactor (ACRR) facility at Sandia, and found to contain relatively more high-energy neutrons. The (normalized) ion diode spectra is compared to that produced by a Cf252 source, and found to be almost identical.

7) **Attempts to characterize neutron dose experimentally** using devices and dosimetry foils are discussed. Initial efforts were compromised by substantial damage cause by beam impingement on the front of the fixtures containing test samples. Attempts to mitigate debris caused by beam damage are discussed, including the design and fielding of a robust beam stop for the "rear"-propagating ion beam.

8) **As part of measurements of personnel exposure**, in particular the Operations Console location (where personnel are required to be present for a HERMES shot), fielding of a device called the "Albatross" [16,17] is described. The Albatross provided key measurements that appear to validate MCNP predictions of neutron dose, and are consistent with a proton beam of peak voltage 16 MeV and 200 kA peak current.

9) **Conclusions and suggestions for future work.**

3. USE OF BEAM-TARGET INTERACTION TO YIELD NEUTRONS

High-energy protons impinging on solid metal foil targets can initiate (p,*x*n) nuclear reactions which yield neutrons. The target geometry is a thin foil which the protons impact at normal incidence. The range of 15 MeV protons in typical metals is slightly less than 1 mm, which leads to the thin foil geometry. In a (p,*x*n) reaction, an incoming proton interacts with a nucleus, giving rise to *x* neutrons. The number *x* is a function of the proton energy. As the proton energy rises, the number of neutrons produced also rises. For the range of HERMES proton energies, x is generally equal to one, although for some elements, like tantalum, the (p, 2n) reaction is accessible. The list of (p,*x*n) reactions is quite extensive, and is cataloged, for instance, in the JANIS Book of proton-induced cross-sections [6]. The listing contains over 800 pages, although the listing also includes non-neutron producing reactions such as (p,α) and (p, γ). One example is shown in Fig. 1a, which plots the (p,2n) cross-section for tantalum. The peak cross-section reaches 1 barn, which is quite high, considering that the maximum yield for the more familiar (d,d) nuclear reaction peaks at one-quarter of this level. In this case, Ta181 is the only isotope, and the daughter product is W180, which yields the abbreviation Ta181(p,2n)W180. W180 is a radioactive isotope, with a half-life of 1.8e18 years, i.e. about the age of the universe. Such a long half-life means that there are very few atomic disintegrations per unit time, the source of observed post-shot activation.

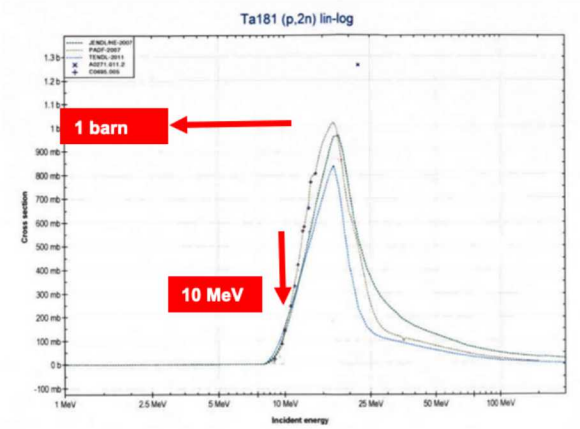

Fig. 1a

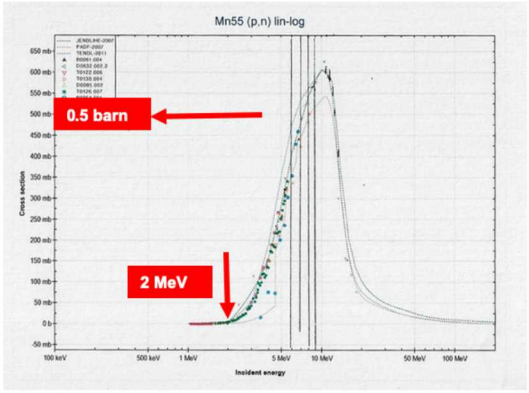

Fig. 1b

There is in fact an additional (p,n) reaction involving protons and tantalum. This reaction peaks at approximately 10 MeV, but with a peak cross-section of only 0.1 barn, about one-tenth of the (p,2n) peak. The daughter product is this case is W181, which is also radioactive, with a half-life of 121.2 days. This could be a worrisome number. A rough rule-of thumb for the number of half-lives before a particular radioactive isotope becomes safe to handle is 8. Therefore, desirable half-lives are either very short (< 1 sec to minutes), or years. If the former, then an isotope rendered radioactive will decay well before it is operationally necessary to remove the material from an experiment in order to prepare for the next shot. This assumes an expected shot rate of say one per day, the goal for these ion diode experiments. If the half-life exceeds one year, then the specific disintegration rate should be well below the threshold for release to the local Radioactive Material Area (HERMES test cell) by Radiation Protection (RP) personnel and away from the diode area. For half-live values in between these limits, the risk of excessive activation should be taken seriously, and evaluated on a case-by-case basis. In the case of the tantalum (p,n) reaction, the risk of excessive activation was regarded as minor, and this was in fact realized in practice, i.e. exposed target samples were approved for RMA release by the morning after the shot.

Examination of Fig. 1a indicates a feature of the (p,2n) tantalum reaction that suggests that a single Ta target of sufficient range to stop incoming protons completely (known as a “thick target”) is not the optimum neutron target to use. This is due to the indicated threshold for the (p,2n), which is ~ 8.5 MeV. This means that for an incoming proton that slows down as it transits the thick target, once the proton energy drops below 8.5 MeV, no further neutron production is possible. A different approach makes use of two *sub-range* foils. The first foil could be kept as tantalum, but the thickness reduced. The amount of reduction is suggested by the plot in Fig. 1b, which shows the (p,n) cross-section for protons incident on Manganese (Mn). In this case, Mn55 is the sole isotope, and the reaction is written Mn55(p,n)Fe55. The cross-section peaks at a lower value than the tantalum (p,2n) at ~ 11 MeV, but the threshold for the reaction is only 2 MeV. Suppose then that a sub-range Ta foil is thick enough so that the incoming protons lose 3-4 MeV as they transit through the foil. Then as the protons strike the second Mn foil, they possess an energy near the peak of the Mn (p,n) cross-section. Then as the protons decelerate further, they can continue to produce neutrons till they reach 2 MeV in energy, instead of 8.5 MeV with the tantalum foil. In this way, a double-foil arrangement of sub-range foils can yield a higher neutron dose than a single thick-target foil. The first foil facing the incoming protons has the higher energy peak in its (p,n) cross section, followed by a second foil with the peak at a lower energy. Candidate metals for the first foil include tantalum (Ta), cobalt (Co), and zirconium (Zr). For the second foil, examples are manganese (Mn) and niobium (Nb). In each case, optimum foil thicknesses are determined from proton stopping powers obtained using the SRIM code [18,19]. Foils of each of the listed metals (except manganese) were fielded during the Project. Operational considerations for foil use include: 1) availability of metal in foil form. Samples for this project were obtained from Goodfellow USA, and were a minimum of 99.9% pure;

2) metals considered need to be of sufficient strength to be free-standing, not oxidized in air, and non-toxic; and 3) metal foils need to be reasonably priced, since they will be used only once.

MCNP simulations were performed of various dual-foil combinations, and results are detailed later in this Report. The neutron outputs were compared to two further examples: 1) thick target tantalum, and 2) neutron output from a standard HERMES bremsstrahlung diode shot. In the latter case, the method of neutron generation is the impingement of the high-energy HERMES electron beam on the normal tantalum converter package used to generate high-energy photons. The resultant photons give rise to neutrons, a process known as *photoneutron* production. Detailed characterization of the photoneutron fluence and spectrum was undertaken by Sanford et al [5]. Data from this paper, as well as data obtained from current bremsstrahlung shots, will be compared to the predicted and measured neutron output from ion diode shots taken during this project.

4. RADIAL DIODE DEVELOPMENT AT HALF-MACHINE POWER (2008-2010)

The radial ion diode that is the platform for neutron generation for this Report was initially developed within a prior LDRD Project, at half-power on HERMES (~ 6 MeV). That earlier work established the basis for successful operation at full-power on HERMES, and will be briefly described.

The beginning baseline for expected diode geometry at half-machine power operation was a) using positive polarity, and b) power flow into not a radial ion diode, but one of *axial* geometry. The advantage of positive polarity operation is that any resulting beam can be extracted into a drift region, simplifying beam characterization. The axial diode design had been successfully used in a number of facilities. In an axial diode, the cathode faces the anode along the beam propagation axis. Figure 2 shows a schematic drawing of the axial diode geometry. The anode (shown here at the end of a positive polarity MITL conductor as operated on HERMES) consists of a disk covered with a thin plastic membrane that acts as the ion source. The cathode tip is located ~ 1 cm away in the z-direction. The resultant ion beam propagates to the right in the drawing, and transits an additional thin plastic foil into a gas cell filled to ~ 1 Torr with atmospheric gas. Electrons flow along the foil in order to charge- and current-neutralize the ions, and the electron current so flowing is measured by a Rogowski coil that acts as an ion current monitor.

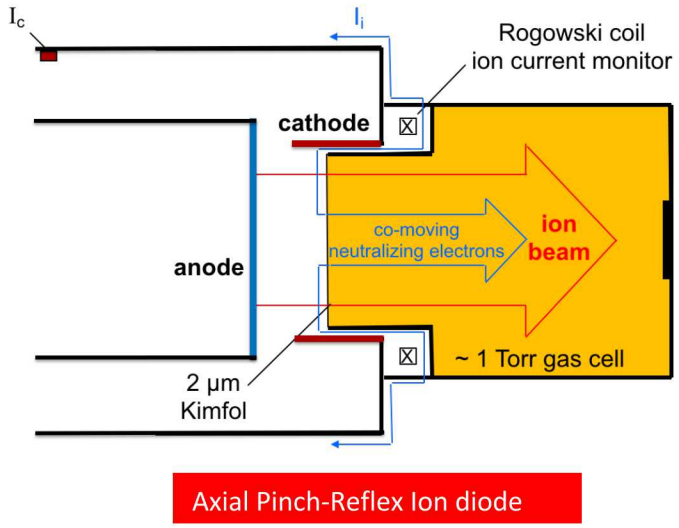

Figure 2

Such axial diodes had been successfully developed and operated, principally at the Naval Research Laboratory (NRL) [20,21]. While the drawing above depicts the anode at the end of a MITL, such a diode as operated at NRL and at other facilities (a converging power version was operated on PFBA-II at Sandia) was connected to the driver by a high-voltage interface instead of an IVA. That is, in the drawing above, the anode was connected to the cathode by grading hardware that can be thought of as a line extension from the anode, both above and below the anode plane, to the cathode conductor. In particular, no current is conducted as electron flow into the vacuum region. In addition, the NRL axial diode design is mated to a driver (Gamble II) [20,21] with a 2 ohm output impedance. To attain a low diode impedance, the cathode tip is located quite close to the anode plane, with the A-K gap much smaller than the anode radius. The cathode-emitted electrons approach the anode quite closely, then are bent by their own magnetic field so as to follow a path that pinches in towards the diode axis. The proximity of the electrons to the anode plane (and even reflexing through the plane) helps to 'turn on' the anode plastic (i.e. gas formation and ionization in a thin layer). The ions are then extracted and flow to the right. With this small-gap geometry, most of the anode plastic is turned on, and ion orbits are characterized by light but not strong pinching on axis as the beam propagates.

On HERMES, both positive polarity operation and the use of the axial diode (optimized for low impedance) were observed to be problematic. The problem of positive polarity IVA operation can be illustrated in Fig. 3 below, which shows a side schematic view of the HERMES MITL, including the upstream adder section, for both negative and positive polarity operation. At each of the adder cavities, the voltage coming forward is increased. (The drawing is simplified to show only 5 cavities, when in fact there are 20.) When the center conductor is pulsed negative (upper drawing), the emitted electron flow (BLUE) follows a relatively smooth path towards the right, whose radial extent is narrow. At the diode (in this case a bremsstrahlung electron diode), the additional diode current (RED) joins the electron flow, across the A-K gap (typically 53 cm or greater). In positive polarity (lower drawing), however, the emitted electron flow is much more complex. This is because at each adder section, electrons are emitted at a higher potential than from the section before, and end up occupying a greater amount of the intra-conductor volume. The various colors representing emitted electron flow depict an electron population that occupies almost the entire volume separating inner and outer conductors. This pattern of flow is known as *saturated* flow [22], which can lower the vacuum output impedance by as much as factor 2, i.e. from the normal 34 ohms in negative polarity to below 20 ohms. The net result is a significant reduction in driver efficiency, independent of what diode load is in place. In the ion diode experiment conducted in positive polarity under the earlier LDRD project, another result was significant current loss coming forward, by as much as 50%. The source of this current loss, which persisted despite changes to the diode geometry, was not understood, and ultimately operation on HERMES in positive polarity was abandoned in favor of negative polarity operation, which proved much more efficient.

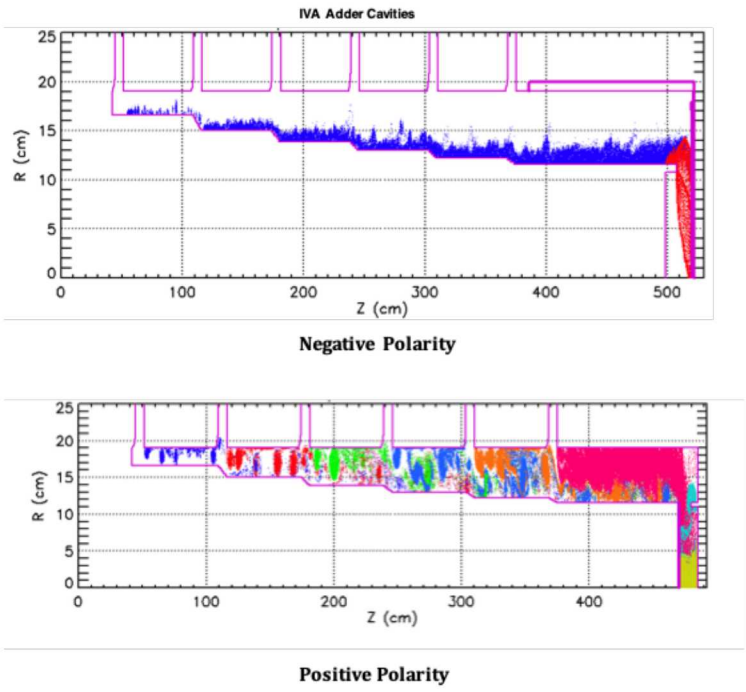

Figure 3

The problem of axial diode operation on HERMES is due to the 34 ohm vacuum impedance of the MITL. This number is significantly higher than the 2 ohms (typical) of previous axial diode operation. To achieve an increase in diode impedance closer to the tens of ohms necessary to couple power efficiently from HERMES, the A-K gap must be increased significantly. As a result the emitted electron flow that approached the anode closely with a small A-K gap now remains further away from the anode plane, except close to the diode axis. It is the presence of electrons in close proximity to the anode plane that reduces space-charge effects and thus increases the current density of the emitted ions. Without the electrons close to the anode, significant ion current occurs only an a small region close to the diode axis, producing in effect a "pencil" beam with poor optical properties. Referring to the geometry in Fig. 2, an ion beam operated at low diode impedance is emitted from a large fraction of the anode plane and propagates to the right, through the Rogowski membrane, and can impinge upon diagnostic hardware placed at the right-hand edge of the gas cell (beige) region. However, a small-diameter ion beam emitted from the near-center anode region, as with a high impedance diode, is likely to overfocus and then disperse outward in radius. Such a beam would never arrive at the right-hand edge of the gas cell, but instead impinge at large radius and with low current density.

This behavior was confirmed in experiments using the diode region design shown in Fig. 2. Witness plates were placed at the right-hand side of the gas cell region. No damage was ever seen on the plates, even after multiple exposures. The witness plate was then replaced by a different beam diagnostic, known as a "shadowbox". This diagnostic consists of two plates, placed one after the other in the direction of beam propagation. The first plate has an patterned array of aperture holes, which define ion "beamlets", which then propagate a short distance to a blank witness plate. A photograph of the shadowbox fielded is shown in Fig. 4 below. The spacing between the plates is 2 cm. After a shot, a set of thin copper straight wires is inserted through the aperture holes until the wires contact the damage spot created by the respective aperture. A collection of such wires presents a visual presentation of the focal behavior of the ion beam. In the Fig. 4 photograph, it can be clearly seen from the position of the wires, that the angle of tilt increases as the radial position of the aperture increases. In other words, the beam appears to be

diverging from a position located above the wire array, i.e. towards the origin of the beam. This supports the picture of a diverging beam that was mentioned in the previous paragraph.

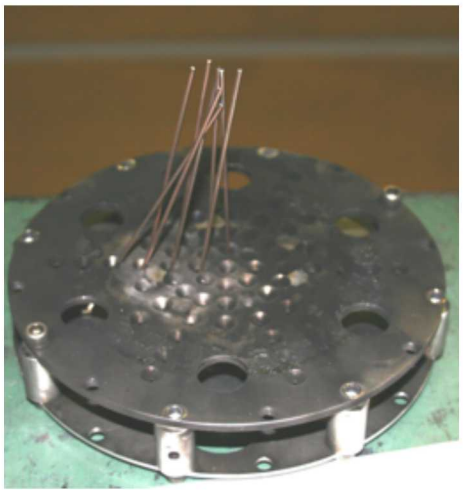

Fig. 4

As a result of the observations above, the design of the ion diode was modified to one that could be operated with HERMES in negative polarity, and with a relatively high diode impedance. The result is schematically depicted in Fig. 5. In the drawing, power flow proceeds from left to right. In normal bremsstrahlung electron beam operation on HERMES, the outer part of the cathode would be terminated, and a planar converter would be placed at the right-hand side of the drawing, at least 53 cm from the cathode tip. To form the modified ion diode for this project, the outer portion of the cathode is extended, but in a direction towards the diode axis. This *radial cathode* (shown in red) then faces an anode stalk that consists of a hollow tube of 7.6 cm outer diameter, which protrudes along the diode axis away from the (right-side) anode plane. The A-K gap is then defined by the spacing between the tip of the radial cathode, and the surface of the anode tube. This distance is a nominal 4 cm, although this was varied slightly during the project. The “anode cone”, shown connected to the right-hand wall, is designed as a field shaper to help guide the electron flow, which in this geometry must reverse its direction.

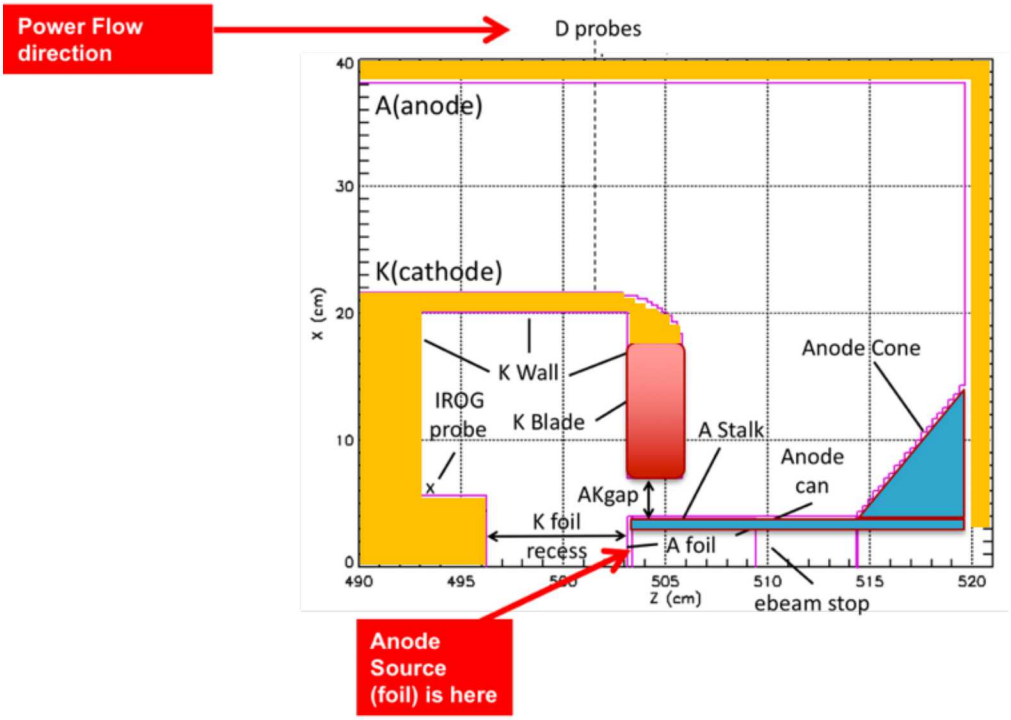

Fig. 5

The geometry of the *radial ion diode* depicted in Fig. 5 is significantly different from that of the axial ion diode shown in Fig. 2. Aside from the radial orientation of the cathode, the A-K gap is greatly reduced from the axial gap in the standard bremsstrahlung electron beam diode normally fielded on HERMES, from at least 53 cm to a nominal 4 cm. One might be expected to conclude that the resulting diode impedance would also be significantly reduced from the bremsstrahlung case. This does not turn out to be the case, although the diode impedance as a function of time is modified from the bremsstrahlung case. This can be best demonstrated by describing the results of LSP modeling of the geometry shown in Fig. 5, which was the setup geometry for the LSP simulations. Such modeling was first performed as part of the earlier half-machine project. Since the particle dynamics, if not the voltages and currents, behave approximately the same for either half- or full-machine operation, the discussion is included in the following full-power section.

5. RADIAL DIODE DEVELOPMENT AT FULL-MACHINE (2017-2019)

5.1 LSP simulations of the radial ion diode

The geometry shown in Fig. 5 was the starting point for LSP simulations of current flow in the radial ion diode. The input current was specified at a location approximately 2 meters upstream of the A-K gap, where there are current monitors on HERMES for both the inner MITL (bound current) and outer MITL (total current). Current waveforms at that location were chosen to match as closely as possible measured current levels on typical HERMES full-power shots, where a full-power total current peaks at ~ 625 kA.

We first discuss the particle dynamics depicted in the simulation results. Particle plots are shown in Fig. 6 for three populations at peak diode power (t = 50 ns): 1) MITL flow electrons propagating from upstream (GREEN), electrons emitted from the cathode (BLUE), and ions propagating towards the upstream direction from the source foil (ORANGE). The electrons, of both flow and diode origin, are observed to execute a rather complex trajectory which at first is directed towards the anode wall in the z-direction. They then bend in a 180-degree arc, and pass between the cathode and anode, turning then radially inward, flowing along and near the surface of the anode foil. It is this indicated proximity of the electron population to the entire anode source foil that is presumed to result in a uniform "turn-on" of the anode plasma in radius, from which the ion beam is extracted. (Damage patterns from witness plates (discussed below) indicate a relatively uniform damage pattern roughly equal in radius to the anode tube diameter.) In this aspect, the electron trajectories more closely resemble those of a low-impedance axial ion diode, as described in the Fig. 2 discussion, than a high-impedance axial ion diode. The bending of the electron trajectories can be ascribed to the effect of magnetic insulation, since there are no external field coils deployed here. At earliest times, the initial electron flow flows almost directly to the anode tube, but the rising current bends the electron path away from the anode side and towards the front of the anode tube. This picture of the electron current flow is consistent with the observed appearance post-shot of the anode tube in the most recent HERMES shots, where it is observed that the anode tube sustains almost no damage.

The final stage of the particle trajectories is also complex. After the electrons turn inward towards the axis and flow toward the anode foil, a segment of the electron population (possibly a substantial segment) proceeds through the foil into the hollow anode tube towards the right. The electron and ion particle plots in Fig. 6 depict particle flows inside this tube all the way to the end of the anode tube. The electrons enter the anode tube after passing through the thin anode foil at full diode energy while the ions are emitted from the back (right) side of the anode foil. These ions are then accelerated to the right in the electric field inside the tube created by the electron beam space charge in an attempt to neutralize this electron beam space charge. Thus, the ions can reach high energy by the time they reach the end of the anode tube. Without the presence of the ions, the electron beam could eventually form a virtual cathode and come to rest before reaching the end of the tube. However, with the ions any virtual cathode (in front of the ions) can continue to the end of the tube as observed in the simulation, pulling the ions with them.

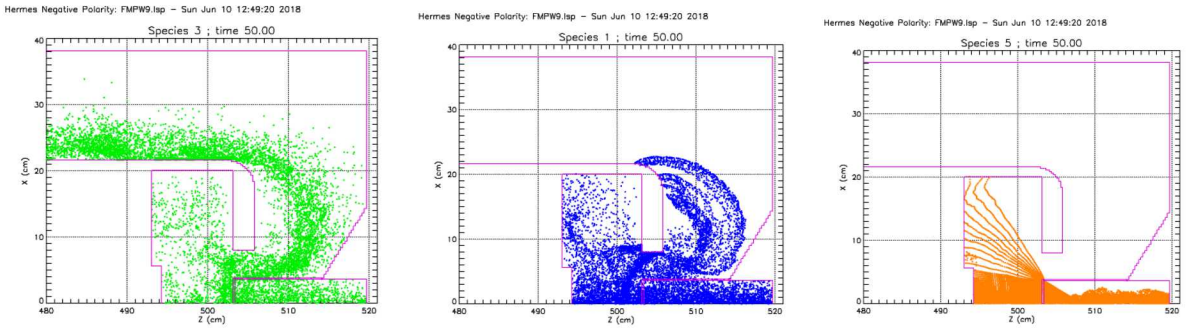

Fig. 6

In experiments, virtual cathode behavior is not observed. An electron beam is observed to propagate along the anode tube interior and strike a witness plate located at the far end of the drawing to the right in Figs. 6. This "rear" intense electron beam is accompanied by an ion beam as indicated in the simulations shown In Fig. 6. In the forward direction, the current consists of full-energy ions in which co-moving electrons are imbedded, so as to preserve net neutral charge. The electrons travel at roughly the same velocity as the ions, but due to the great difference in mass, possess only about 1/40 of the energy. (Velocity scales as the square-root of the particle mass.) However, in the "rear" direction, the electrons, having fallen through the full diode potential as they pass through the anode foil, have high velocity (near

the speed of light), and are thus capable of generating bremsstrahlung and activation if impinging upon high-atomic weight anode targets at the right at the end of the anode tube. The neutralizing ions are emitted from the back side of the anode foil with zero energy and accelerated to an undetermined energy in an attempt to charge neutralize the electron beam space charge. However, this ion energy can be significant. This was demonstrated anecdotally on a full-voltage shot, when a small amount of material composed of steel alloy were placed in the target path of both forward and rear beams. Considerable activation was observed in both beam targets, implying that some fraction of the rear ion population must have exceeded 10 MeV. Thus, in principle, the "rear" beam could be a second source of high-energy protons for neutron generation. This point will be revisited in detail below.

In addition to the prediction of two ion beams, the most significant result of the LSP simulation depicted in Fig. 6 is the prediction of complete incorporation of the MITL electron flow into the diode as part of the total current. In a self-field diode, the ion efficiency is a function of the total diode current, so maximization of ion current is best satisfied when all of the MITL current is included in the current flow. A principle technique used to produce current incorporation is to ensure that the diode impedance is less than the self-limited flow impedance of the MITL. For an IVA like HERMES operating in negative polarity, the self-limited flow impedance is approximately 75% of the vacuum impedance (34 ohms). To assess the diode impedance of the radial ion diode, we can compare the measured total and bound currents on an ion diode shot at the position 2 meters away (z = - 2 meters) from the A-K gap, as previously mentioned. For additional perspective, the ion diode waveforms are compared with total and bound currents from two standard HERMES bremsstrahlung shots in Figs. 7a and b below. The total and bound current waveforms for three HERMES shots are shown in Fig. 7a, where the ion diode total and bound currents are colored WHITE and OFF-WHITE, respectively. The main difference between the ion diode and bremsstrahlung waveforms is the rapid rise in the bound current (labeled as retrapping wave) for the ion diode shot, just past peak current. This rise signals the arrival of the retrapping wave from the diode, indicating coupling to a diode impedance that is lower than that of the self-limited flow. Since the A-K gaps are so much larger for the bremsstrahlung shots, the diode impedance is higher than for the ion diode case, and there is no retrapping wave reflected from the A-K gap on those shots.

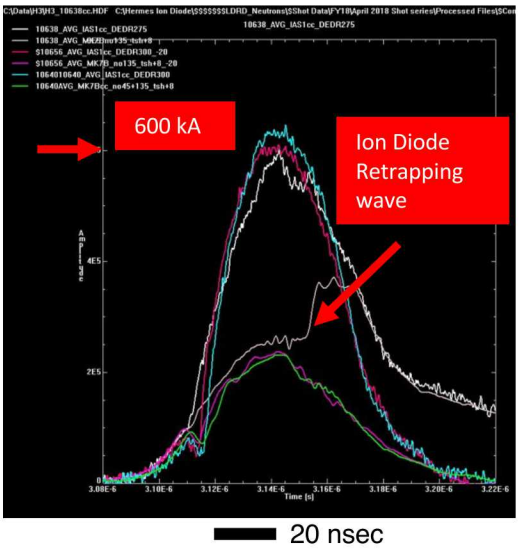

Fig. 7a

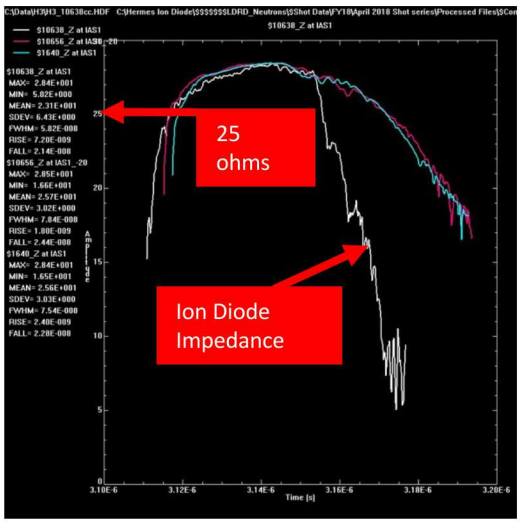

Fig. 7b

The impedance can be calculated at the point 2 meters upstream of the A-K gap (z = -2 meters) by first estimating the MITL voltage at this point. The voltage can be calculated using the currents obtained from

the total (outer) and bound (inner) current monitors using the theory of Miller and Mendel [23,24], as modified more recently [25,26]. The form of the Mendel Equation used for this paper is given by an expression from Reference 25:

$$V_{MITL} = Z_0(I_a^2 - I_c^2)^{1/2} - [(gmc^2/2e)(I_a^2 - I_c^2)/I_c^2] \qquad (1)$$

where I_a denotes the total current measured at a particular point in the MITL, I_c denotes the bound (cathode) current at the same axial location, Z_0 is the MITL vacuum impedance, and g is a parameter of order 1. (If g = 1, the original Mendel equation is recovered.) The value of g is determined from particle-in-cell (PIC) simulations, and for an output voltage of ~ 18 MV, g is determined to be ~ 1.2. Accordingly, this value of g is assumed for analyses in this paper. In practical terms, the difference between a g value of 1 and 1.2 amounts to < 0.5 MV difference in the calculated voltage. The impedance at the upstream position is then calculated by dividing V_{MITL} by the total current at that point, as a function of time. The calculated impedance waveforms for the three HERMES shots is shown in Fig. 7b. The impedance waveform for the ion diode shot (WHITE) is observed to follow the two bremsstrahlung shots very closely, until the arrival of the retrapping wave at the time indicated in Fig. 6a, after which the waveform values decline quickly. Thus, prior to the retrapping wave arrival, the line impedance at the position 2 meters upstream of the diode tracks the bremsstrahlung shot behavior quite closely. All three curves reach a soft peak of ~ 28 ohms, which is consistent with the 75% estimate for the flow impedance for a 34-Ohm vacuum IVA. After this time the line impedance drops, indicating the effect of the lower impedance ion diode load compared to the higher self-limited impedance bremsstrahlung diode load. This ion diode load itself is always lower than the bremsstrahlung diode load impedance, but its effect upstream is not observed until the arrival of the slow-moving retrapping wave at the upstream location.

The current monitors at z = - 2 meters were the closest current monitors to the ion diode A-K gap, although closer monitors were fielded for a few shots near the end of the Project. We can get an estimate of the diode voltage, current, and impedance by looking at the LSP simulation results, which predict these waveforms, given the appropriate input waveforms at z = - 2 meters. The simulation total and bound currents, intended to match as closely as possible the total and bound currents for the ion diode shot shown in Fig. 7a, are depicted in Fig. 8. In this plot, I_A is the total current at the 2 meter position, I_C is the bound current, and I_{flow} is the difference between the two, i.e. the electron flow current. As can be seen, when the retrapping wave arrives, the result is that the electron flow is recaptured and flows in the inner conductor. Comparison of I_A and I_C with the respective measured ion diode waveforms in Fig. 7a shows that the simulation overestimates the magnitude of the retrapping wave peak, with the bound waveform rising to equal the total current after peak current. The measured bound current also rises to equal the total current, but only later in time, when the total current itself is reduced. This overestimate of the bound current has implications which will be discussed in detail later.

With these setup currents at z = - 2 meters, voltages and currents at the diode load are then output as simulation results, and are shown in Figs. 9a and 9b. Predicted currents at a location just upstream of the diode (labeled as “D probes” in Fig. 5) are shown in Fig. 9a, with current labels analogous to Fig. 8. It can be seen that the total current I_A peaks at a significantly higher value near the A-K gap, at ~ 800 kA compared to a little over 600 kA at z = - 2 meters. I_C contains no retrapping wave, because it is located very close to the A-K gap, and I_{flow} is considerably reduced from its value at Position D. The total current rises near the load due to the reduced load impedance compared to the MITL impedance. The predicted load voltage can then be expected to be lower than at Position D, and this is confirmed by the waveforms

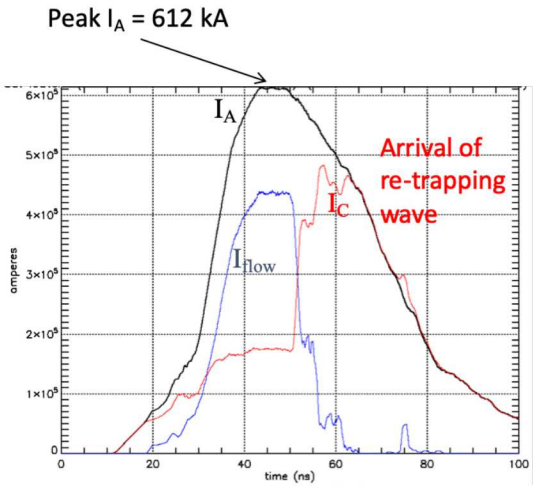

Fig. 8

in Fig. 9b. In this Figure, the V_5 waveform (voltage at Position D) peaks at ~ 16 MV. At z = - 1 meter, the peak voltage has dropped slightly. From this point to Position D and the diode itself (V_D and V_{AK} in Fig. 8b), the voltage is observed to drop to ~ 13.5 MV peak value. This is consistent with the load current rising to 800 kA. It can be also seen that V_D and V_{AK} are more symmetric in shape with respect to rise and fall times, compared to the V_5 waveform. This is because the retrapping wave at z = - 2 meters results in a relatively fast drop in the MITL voltage at z = - 2 meters as a function of time.

With the predicted load voltage and diode current as shown, the diode impedance can be estimated. We take the point of peak V_{AK}, which occurs slightly before the load current has peaked. Thus, the peak diode impedance is estimated at 13.5 MV/750 kA, or 18 ohms. This value is significantly lower than the 28 ohms for the upstream MITL impedance mentioned above. With this simulation geometry, it is seen that for a load impedance at approximately 65% of the upstream MITL impedance, the MITL electron flow is observed to be completely incorporated into the diode current. Additional simulations, in which the A-K gap was varied by ± 1.5 cm, resulted in little change to the predicted diode voltage.

The LSP-predicted diode voltage (~ 13.5 MV) served as the reference voltage for the MCNP calculations of neutron output discussed later in this paper. For those simulations, an estimate of beam current, and specifically proton current, must be provided. The LSP simulations at half- and full-power predict a peak ion current of ~ 60 kA and 120 kA, respectively, propagating in the "forward" direction (i.e. towards the left in Fig. 5). The simulations do not distinguish the type of ion. Previous experiments using such plastic foil ion sources typically report a mixed beam propagating from such hydrocarbon sources, with the proton component estimate as low as 70% of the total, but also observed to be as high as 90% of the total current [27], the remainder consisting of various charge states of carbon. Since the carbon component does not give rise to neutron output, we concern ourselves only with the protonic portion of the ion beam. An approximate starting point for the MCNP simulations would then assume a proton beam of peak current ~ 100 kA.

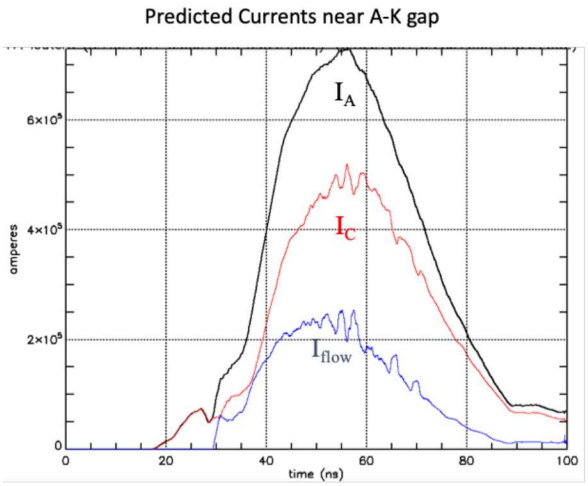

Fig. 9a

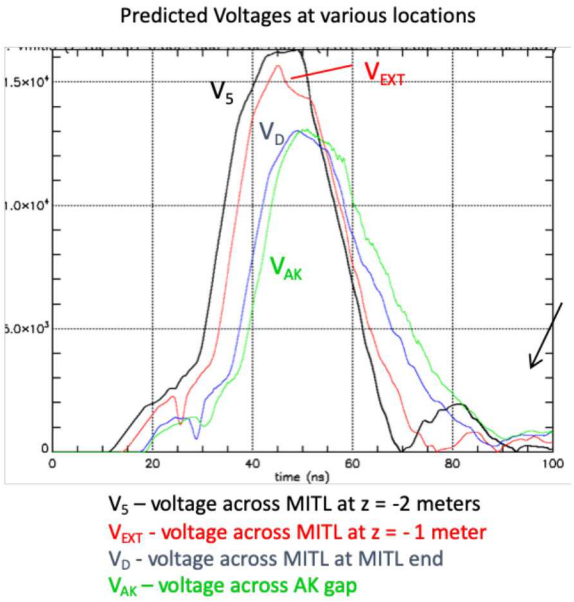

Fig. 9b

6. CHARACTERIZATION OF ION BEAM PROPERTIES USING FARADAY CUPS, ROGOWSKI COILS, AND CALORIMETER

The LSP simulations discussed in the previous section predict a "forward" proton beam current of approximately 100 kA. This amount of current is contained roughly within the 3 inch outer diameter (OD) of the anode tube (see Fig. 5). The simulations also predict a current density peaked on axis, but not pinched. Accordingly, 100 kA figure averaged over the 3 inch OD (7.6 cm) of the anode tube represents a lower bound on the proton current density. This value is = 100 kA/45.4 cm^2 = 2.2 kA/cm^2. This represents a very high proton current density, one that makes direct measurement of the proton current by conventional beam diagnostics such as Faraday cups quite challenging. To get an approximate idea of the effect of such a beam impinging directly upon diagnostics surfaces, consider that the range of 14 MeV protons is ~ 1 mm. A proton beam of peak energy 13.5MeV and peak current of 100 kA deposits ~ 40 kJ of energy over a pulse of full-width-half maximum (FWHM) of 25 ns. Assuming a slight expansion of the beam footprint, say 3.5 inches, then deposition of this energy amount into 1 mm results in a specific energy density of 6.3 kJ/g. If aluminum is used as the (flat) target plate, it takes about 1.3 kJ/g to completely vaporize aluminum. This amount of energy is reached at approximately 30% of the power pulse duration. If tantalum is used as the beam target surface, survivability is certainly better, but some amount of ablation still occurs.

The ablation problem was recognized in previous experiments with high-intensity ion beams such as Proto-I and PBFA-II. One way around the ablation problem is to use the concept of Rutherford backscattering [28]. In this technique, a very thin gold foil is placed in the beam path. During the ion pulse, a small amount of ions are then scattered by the foil out of the beam path, where they can be collected and analyzed by, for instance, impingement on CR-39 and subsequent counting of beam tracks [10,11]. The gold foil itself is of course destroyed, but not before the requisite ions are backscattered to the counting location. Even if budgetary restraints could allow for the fielding of such ion diagnostics, an

examination of Fig. 5 shows that the volume possible for fielding is quite small. This is a direct consequence of the use of negative polarity for the IVA operation, which is a requirement for co-existence with the predominant bremsstrahlung electron mode. Accordingly, the use of simpler ion diagnostics was employed for this Project. We review each of the diagnostics in turn, and discuss the results. The conclusion in each case is only a very qualitative estimate of beam current. It was due to these problematic results that the decision was made to move from direct measurement of ion beam properties to the measurement of the neutrons generated by the ion beam, through the use of dosimetry foils placed in a test fixture that replaces the ion diagnostic fixture.

6.1 Shadowbox/witness plate technique. This was previously discussed in the Section above on half-machine power. The propagating ion beam strikes a series of two plates placed normal to the beam path. The first plate contains an array of aperture holes, which define 'beamlets' that propagate further till they strike a blank witness plate. The separation distance used was 2 cm. By aligning a set of thin copper straight wires through the apertures and aligning with respective damage spots made on the witness plate, one can get a qualitative eye of the beam footprint and propagation behavior. For full-power experiments, a new shadowbox front plate was fabricated out of tantalum, with holes spaced in a radial pattern 0.75 cm apart. The aperture holes were 1 mm in diameter, and were placed at the bottom of a shallow counter-sink. A photograph of the front plate after a shot is shown in Fig. 10a. Besides the general degree of beam damage to the Ta surface that is evident, there are light-colored spots of irregular shape distributed across the surface. These are melted fragments of the plastic anode foil. Across the middle of the plate is a darker area, which is of greater vertical extent on the left-hand side. While the origin of this feature is unknown, the event that caused this must have occurred during the high-energy portion of the proton pulse. This is made evident by a photographic close-up of the back-side of the aperture plate, shown in Fig. 10b, which shows the area directly behind the dark zone. There is clear evidence of rear spall along the middle row of aperture holes, which could have only been made by a high-power ion beam.

A photograph of the aluminum witness plate for the same shot is shown in Fig. 11. While there is some correlation of the damage spots in the photograph with the centrally-located dark area and spall spots, the more important observation is the relative scarcity of damage spots across the 3-inch diameter plate. Subsequent damage observed on plates placed in front of the test fixture later used in this Project show much more uniform damage across the diameter where the aperture plate would be located. The most likely explanation for the inconsistency in damage seen between the witness plate and the text fixture front is what is known as "hole closure". A high-power beam incident on a material plate will ablate the front surface, producing a plasma in the process. When an aperture hole is struck in this manner, the expanding plasma in and near the aperture hole interferes with the beam's ability to transit the aperture. The propensity for hole closure increases with the power of the incident beam. As will be discussed in the section below on Faraday cup measurements, such cups which could give accurate measurements of a lower-power ion beam, such as operated on the RHEPP-1 facility [12], appear to fail partially or completely. The cause can be ascribed to the same hole closure as mentioned here. Thus, the shadowbox/witness plate diagnostic failed to give a reliable image of the incoming beam as operated on HERMES.

Fig. 10a

Fig. 10b

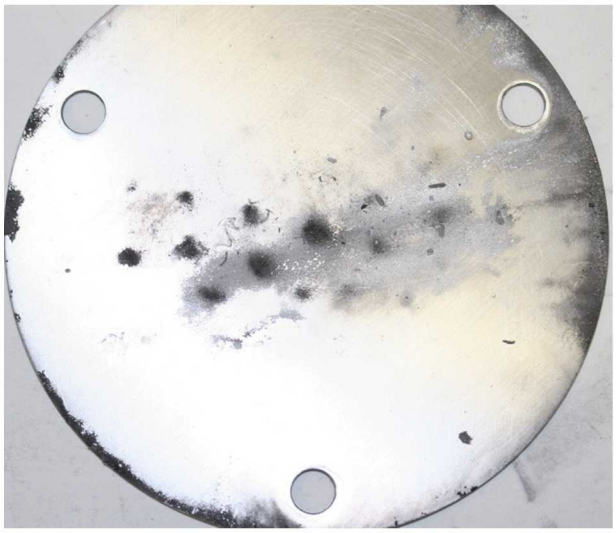

Fig. 11

6.2 Faraday cups. Faraday cups are an estimated method for measuring ion current from ion diodes [29]. Two types of Faraday cups (Fcups) were fielded in experiments during this Project. Both types were used to measure ion current during experiments in half-power HERMES experiments [14]. Individual versions of a small Faraday design originally built for use on RHEPP-1 [12] were fielded on several HERMES shots. They featured an unbiased design, with permanent magnets mounted behind the 1.5 mm-diameter aperture. The magnets are designed to suppress both the electron population co-moving with the incoming ions, and low-energy secondary electrons emitted from the cylindrical cup itself when struck by the incoming ions. These smaller Fcups were previously calibrated [30] by validating against a measured melt duration (Si surface melting measured by laser reflectometer) and 1-D heat flow modeling, at energy fluences up to 2 J/cm^2 (50 A/cm^2 typical current density). A second and much larger Fcup was used also, this larger cup containing a much larger magnet, and 3.2 mm aperture hole. This Fcup was specifically designed for more intense beam measurements [31] than the smaller RHEPP-1 Fcups, which typically recorded at most 300 A/cm^2.

As observed in the previous half-power ion beam experiments, both Fcups gave signals that were not well understood. Examples of such signals are shown in Fig. 12. A scaled MITL voltage (calculated at z

= -2 meters) from Shot 10417 is shown (WHITE) to illustrate relevant times during the pulse. Two smaller Fcups were fielded to sample the "forward" ion beam (RED and CYAN), and the single larger Fcup sampled the "rear" ion beam (BLUE). (Space considerations precluded fielding more than one large Fcup at a time.) The "forward" Fcups indicate a positive-going signal of peak magnitude ~ 1.5 kA/cm^2, consistent with the expected intense ion beam in that direction. The "rear" signal peaks slightly higher, at 1.6 kA/cm^2, and is negative-going, also consistent with the expected rear intense electron beam. But all three signals are of relatively short duration, and have short-term oscillations within the main signal. Time-integration of any of the signals does not yield an inferred transferred charge consistent with a simulation-predicted 100 kA forward-going proton current. There can be several reasons for this behavior: 1) hole-closure of the Fcup apertures, the same process as described above), and 2) a non-uniform current density as a function of azimuth and radius. This can be caused by an ion beam consisting of individual beamlets, which then may impinge on a particular aperture hole, then move away from it. While beamlet formation has been observed in previous ion beam experiments, the qualitative picture suggest by the Fcup data in Fig. 12 is inconsistent with observed beam damage to the front of the test fixture plate (discussed below).

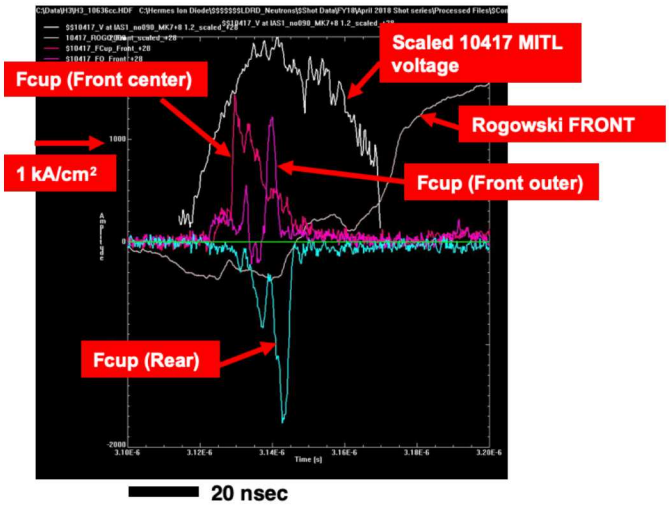

Fig. 12

6.3 Rogowski coil to measure total ion current. The principal of Rogowski coil operation was discussed in the section of half-power experiments. For the radial diode experiments, a thin aluminized mylar foil was located in front of the anode tube and held in place by the beam diagnostic hardware. A waveform from one of the shots in which the Rogowski was fielded is included (OFF-WHITE) in Fig, 12. The signal is at first negative-going, then switches to positive-going, eventually reaching an indicated 80 kA, but only late in the pulse, long after the voltage pulse has subsided. Like the Fcup signals, the Rogowski diagnostic thus gave conflicting results.

6.4 Calorimeter for measuring heat deposited by the ion beam. For this diagnostic, an aluminum plate is mounted so as to face the incoming ion beam. On the back of the plate are mounted several calorimeters constructed of thermocouples, one at the beam axis, and one mounted at larger radius. A third calorimeter is mounted away from the beam, on the side wall of the outer cylinder that holds the front aluminum plate in place. This third calorimeter thus acts as a "null" measurement. A photograph of the aluminum plate, which is 1.3 cm-thick, is shown in Fig. 13a. The photograph shows a series of conical holes drilled into the aluminum in a radial pattern. The purpose of the holes is to attempt to

reduce anticipated surface ablation caused by the incoming intense beam. The hoped-for goal is that the ions, instead of ablating material which is then blown back and away from the plate, will enter each cone and spread their energy over the slanted cone surface, thus reducing the effective energy deposition. In addition, any material ablated would then be propelled forward instead of backward, thus remaining inside the cone. Also, the bottom of each cone is located close to the backside of the plate and closer to the location of the active calorimeters, thus possibly improving their response time.

The colorimeters were calibrated by recording their response to a range of temperatures in a portable oven. Signals from the three calorimeters fielded on Shot 10636 are shown in Fig. 13b. The signal time-scale is quite long compared to the shot waveforms previously shown. The signal from the "null" calorimeter mounted on the sidewall is zero. The signals from the other two calorimeters are non-zero, with the calorimeter mounted further out from the axis registering a bigger signal than the center calorimeter. The bigger side colorimeter peaks at approximately 1 volt output. This can be compared to the expected temperature rise from an ion beam of peak energy 13.5 MeV and peak ion current of 100 kA. The expected temperature rise is approximately 4 volts.

Fig. 13a

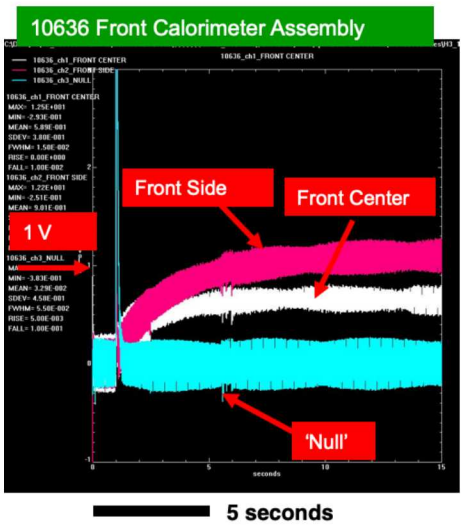

Fig. 13b

An explanation for the discrepancy between the expected 4 volt signal, and measured ~ 1 volt signal, is suggested by the photographs in Fig. 14. The left-hand photograph shows the aluminum plate, shown pre-shot in Fig. 13a, after exposure to two ion beam pulses. The right-hand image is a closeup of the center of the plate. Within each cone can be seen a slight step-in, where the diameter of the hole is observed to decrease. The bottom of the step-in is approximately 1 mm, or about equal to the proton range at peak energy. It can be seen that the plate is heavily damaged by beam ablation. And since the material ablated is heated to the highest temperature, it is not surprising that the measured plate temperature rise is less than the calculated estimate. Thus, the performance of the calorimeter assembly is compromised by beam ablation. Due to the deposition of shot debris on the plate surface (not easily removed), the plate could not be simply weighed after the shot to determine the amount of ablated material missing.

Fig. 14

Taken together, the usefulness of the data from the ion beam diagnostics discussed above is quite limited. The shadowbox/witness plate performance appears compromised by possible hole closure. The calorimeter appears compromised by beam ablation. The Fcup data suggests peak currents in the 1.5 kA/cm^2 region, but for insufficient lifetime to be consistent with the 100 kA proton current estimate. The Rogowski coil indicates a peak current of ~ 80 kA, but in a time-scale not consistent with the beam FWHM.

The decision was made to move on from attempts to measure ion beam properties to measure the effect of the ions on neutron targets, i.e. neutron dosimetry measurements.

7. DEBRIS MITIGATION

The generation of beam debris was expected to be a significant question when HERMES operation was switched to full-power shots from the previous half-power. While the diode hardware would need to be re-enforced to withstand the full beam power, the extent of re-enforcement needed was not known. We first describe the damage level seen in the half-machine HERMES shots taken under the previous Project. For example, beam witness plates used at that time were composed of stainless steel shimstock (activation was not a problem at 6 MeV operation). Photographs of a shadowbox/witness plate diagnostic made from such shimstock are shown in Fig. 15. The left-hand side shows the front surface pre-shot, the middle the front after a shot (8839), and the right-hand side the back side of the witness plate. The front and back plate images show a hole approximately 2 cm in diameter blown through both plates. In addition, the force of the beam bent both plates out-of-plane, ensuring that the procedure for inserting the thin copper rods could not be used. This then was the maximum attained beam damage observed at half-power HERMES operation.

By contrast, we show in Figs. 16a and b the level of diode damage from a full-power shot. The left-hand image (Fig. 16a) shows an anode tube (see Fig. 5) from one of the early Project shots taken in April 2017. The tube was composed of 1/8 inch-thick (0.31 cm) aluminum 6061, of OD 3 inches and length approximately 6 inches long. The tube post-shot is observed to be largely vaporized and remnants re-

deposited on the anode cone. There was additional aluminum deposited in fragments in the general diode vicinity (not shown). The mitigation in this case was to replace the aluminum tube with a thicker (1/4 inch or 0.60 cm) tube made of type 1026 cold-rolled steel, a photograph of which is shown (post-shot) in Fig. 16b. The (outer) tube is dark-colored due to blowback from the cathode hardware (not shown). The tube can be seen to be undamaged, and could be used again. While the use of steel on the anode-side does not lead to activation, there is a possibility that the electron beam propagating along the axis of the tube could spread outward and contact the inner diameter of the steel, causing an activation potential. For this reason, an inner lining tube of aluminum (light-colored in the photograph) was mounted to eliminate this potential.

Fig. 15

Fig. 16a

Fig. 16b

Another source of debris was the two plastic foils used in the experiments. The smaller one acted as the ion beam source, and the larger aluminized mylar was used in conjunction with the Rogowski coil. The beam source foil was originally made of a plastic called Polyethylene terephthalate (PETG), which was used in the previous half-machine project. In addition, there were two aluminum aperture plates (0.5 inch-thick), behind which the beam diagnostics were deployed. These plates were damaged, and ablated aluminum material was blown back into the A-K gap. With the decision to remove beam diagnostics in favor of the text fixture hardware, the aluminum plates and the aluminized mylar foil were retired. The PETG foil continued to be used until the last year of the Project (FY2019), when it was replaced with a (thinner) polyethylene foil. This was due to the reduced propensity of the polyethylene foil to form *char* [32], that is, macroscopic balls of melted plastic that could be seen after a beam shot.

The polyethylene foil use resulted in the elimination of plastic debris for the FY2019 shot experiments (the aluminized mylar having already been removed). There was, however, an unexpected possible side effect that may be ascribable to the use of the polyethylene. Comparing the FY2018 to the FY2019 shot experiments, there appeared to be an anecdotal increase in beam power. More details will be given below. The ½ inch-thick aluminum plates mentioned above and used as aperture plates in front of the ion beam diagnostics in FY2018 were damaged after each shot, but re-usable. In FY2019, up to ¾-inch thick aluminum thickness was penetrated by, in particular, the "rear" (electron) beam. This is an order-of-magnitude increase in beam damage, and had significant impact on the deployment of dosimetry samples to measure neutron dose in FY2019. One possible reason is that more protons could be extracted from the polyethylene than from the previously used PETG plastic, i.e. that the PETG was a somehow source-limited ion source. This seems improbable, as the sheer number of protons in the plastic would seem to be able to provide enough protons for a serviceable ion beam in either case. Given the lack of other factors contributing to the observed increase in beam power, however, the change in plastic remains a possibility.

The use of steel for the anode tube, and switchover to polyethylene for the source foil contributed significantly to debris mitigation in the beam experiments. However, there is one last area of beam debris that must be mentioned. We describe here in more detail the change (and simplification) of the diode hardware that occurred in the change from beam diagnostic fielding to the test fixtures. With both the front and rear beam diagnostics packages in place, a conceptual 3-dimensional drawing of the diode region is shown in Fig. 17. In this drawing, the HERMES accelerator is out of view towards the right, and only the MITL section closest to the diode are shown for clarity. The anode tube is shown in lavender, and the (radial) cathode in turquoise. The forward (right) diagnostics package is shown attached to the cathode by an outer flange, and the rear (left) attached behind the anode cone. In this hardware arrangement, the principle source of debris was blowback from beam ablation of the two aluminum aperture plates placed in front of the beam diagnostics (not shown in the drawing for clarity).

For the switch from beam diagnostics measurements to deployment of neutron dosimetry foils in the test fixtures, the fielding geometry switched to that shown in the schematic drawing in Fig. 18. The drawing focuses on the front (right) test fixture, depicted as an upright cylinder with interior space shown in yellow. The front portion of the anode tube is shown (BLUE), along with the radial cathode (hashed). In the original design, the front plate of the test fixture was made of 1/8 inch-thick aluminum. The neutron target foils were mounted on an additional 1/8 inch-thick aluminum flange, and held in place with an outer flange ring. A similar but smaller test fixture (not shown) was located so as to intercept the rear (left) beam, with the front plate of this fixture made of 3/8 inch-thick aluminum.

The first fielding of the two test fixtures occurred in the FY19 test series in June 2019. In retrospect, the switch to the test fixtures coincided with the observed (and as yet unexplained) significant increase in beam power. The extent of the increased beam power can be seen in photographs taken of the front and rear test fixture covers shown in Figs. 19a and b, respectively. These photographs were taken after the *second* of two shots taken. The front test fixture photograph (Fig. 19a) shows the remains of the neutron targets (bright annulus), and within the annulus the remains of the aluminum target mounting plate. Not

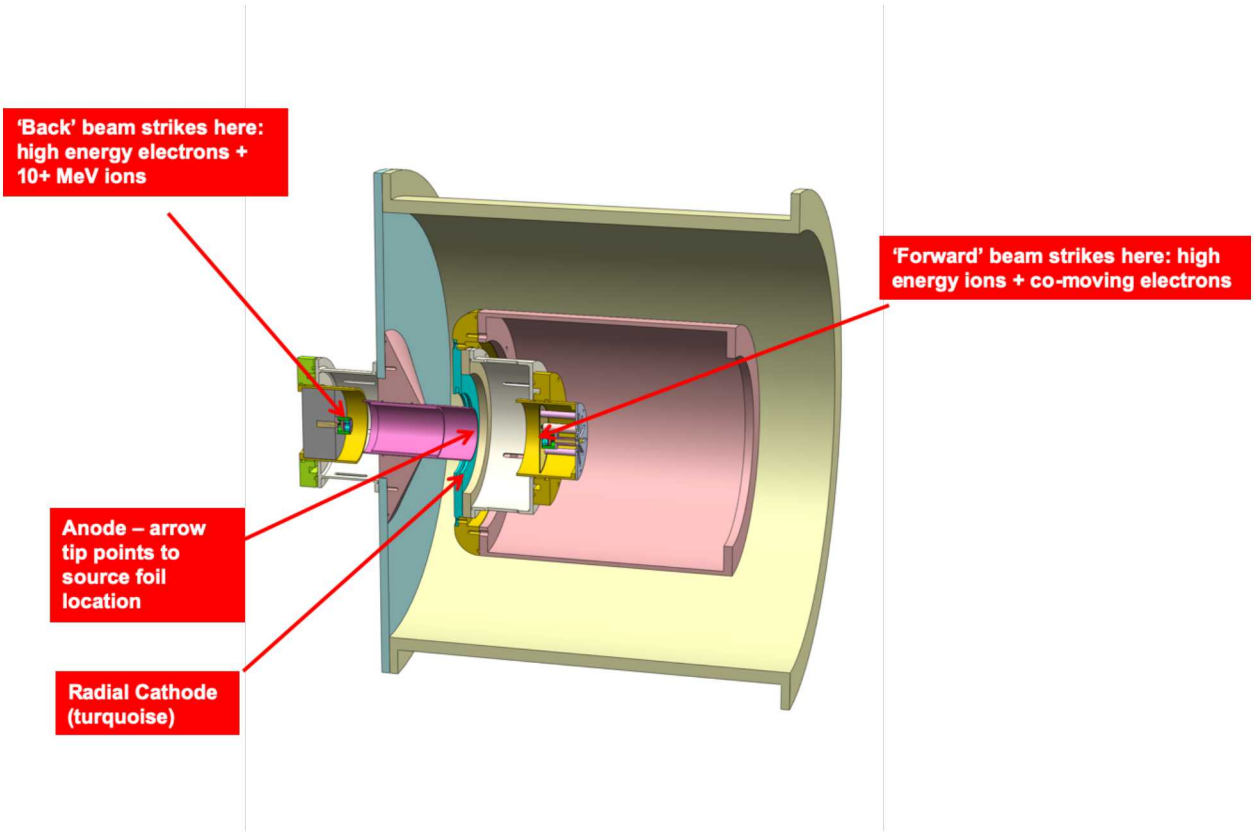
'Back' beam strikes here: high energy electrons + 10+ MeV ions
'Forward' beam strikes here: high energy ions + co-moving electrons
Anode – arrow tip points to source foil location
Radial Cathode (turquoise)

Fig. 17

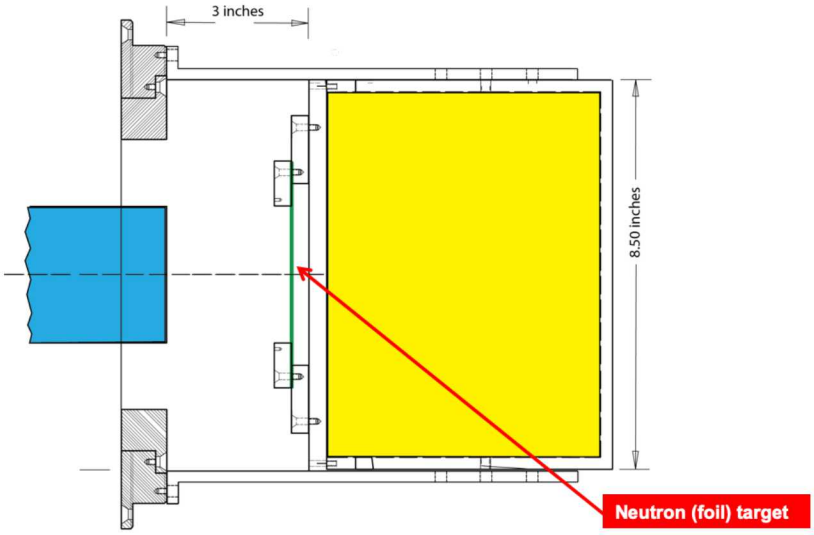
3 inches
8.50 inches
Neutron (foil) target

Fig. 18

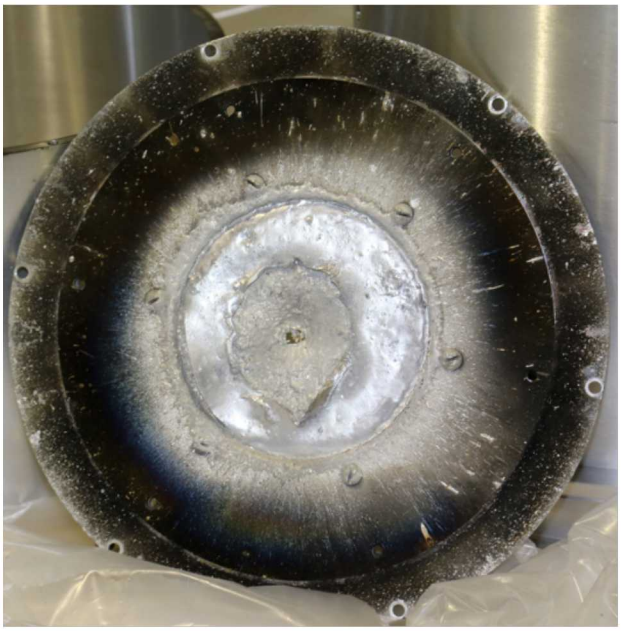

Fig. 19a

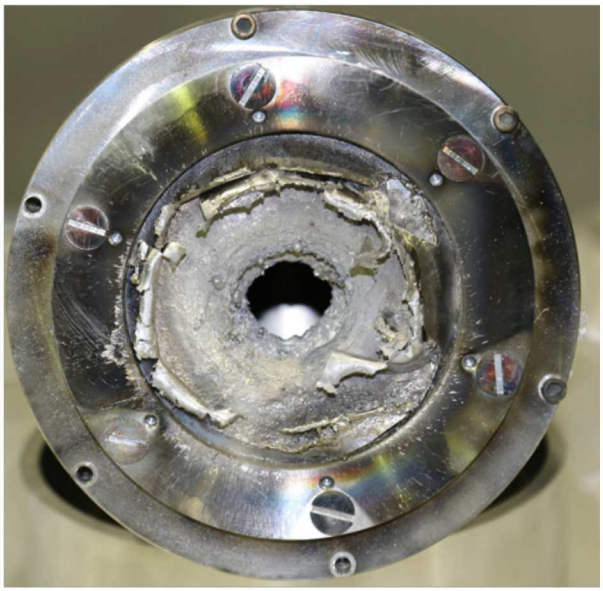

Fig. 19b

quite visible in the photograph is a small penetration in the target mounting plate, behind which the test fixture front plate remained undamaged. In the case of the rear test fixture (Fig. 19b), the remains of the neutron target are shown peeled back towards the outer capture bracket, and in the middle is a hole of size ~ 2.5 cm, through which the interior of the test fixture can be seen. The hole shown extends through *two* 3/8 inch-thick aluminum plates, a total distance of ¾ inch (1.9 cm).

While the damage seen is notable enough, this was the second of two shots taken with this geometry. On the first shot, only the front test fixture plate (1/8 inch-thick aluminum) was in place, and only one of the 3/8 inch-thick aluminum plates was in place for the rear test fixture. On this first shot, the vast majority of the dosimetry foils and devices (55 in all) were mounted. Both test fixture plates were penetrated on this first shot. As a result, all the mounted samples were compromised by possible direct proton strikes in addition to any neutron flux from the neutron targets, making an post-shot analysis difficult. Only a relative handful of dosimetry foils (4 in total) was fielded after the first set of shots.

The mitigation for the front test fixture (Fig. 19a) was to replace the aluminum front fixture plate with a tantalum plate of the same thickness (1/8 inch). This stopped the beam penetration into the front test fixture. Remaining beam debris was confined to the neutron target itself. The extent of the reduced damage and debris can be seen in Fig. 20. This is a photograph of the neutron target taken after the last ion diode shot of the Project (September 2019). The neutron target consisted of a tantalum foil followed by niobium, with additional 10 mil-thick tantalum foils underneath (to increase survivability). The two top foils, and two of the 10 mil tantalum foils were melted, but the remaining 10 mil foils plus the tantalum test fixture plate were undamaged. The radial extent of the damage was limited to barely more

than the foil diameter (3.6 inches) itself. The inner bolt circle holding the foils could still be loosened after the shot. Almost no debris was observed away from the target area itself.

Fig. 20

The mitigation of the rear text fixture debris was more complicated. One conclusion that may be inferred from seeing the damage in Fig. 19b is that no practical thickness of aluminum can withstand the augmented rear beam power. Neither steel nor tantalum can be used for the rear assembly, due to activation concerns. The decision was then made to abandon the rear test fixture, since any test samples mounted within could not be protected from beam penetration into the test cell. Then the volume of the rear test fixture could be replaced with a different beamstop design, one that removed the potential for ablated material to be blown backward into the A-K gap. The new beamstop design is shown schematically in Fig. 21a, and photographed as fabricated in Fig. 21b. The incoming rear beam enters the hardware from the right-hand side, and encounters a cylindrical cone, the outer diameter of which is slightly larger than the beam footprint. The purpose of the cone is to diffuse the beam ablative power, since the beam fluence (in J/cm^2) are spread over a larger distance than the original flat geometry. And what material that does get ablated now is propelled forward (i.e. to the left), instead of back into the A-K gap. At the bottom of the cone is a 0.5 inch hole, through which ablated material is transported into a separate “get lost” region (defined by the piece outlined in red in the drawing). The rear (left) surface of this region has a surface profile that is slanted away from the incoming beam material, i.e the height at the axis is higher than for points further out in radius, this to divert incoming material towards the sides of the get-lost region. The central part of the rear surface (BLUE) is replaceable.

The fielded beam stop was completely successful. After a shot, the hardware was disassembled, and the collected aluminum debris was observed to be in loose balled-up form, and easily removed. The beam stop was then reassembled and ready for the next shot. The use of the new rear beam stop eliminated the occurrence of aluminum debris in the A-K gap region. Thus, the combination of steel for the anode tube, polyethylene for the ion source foil, migration to a forward test fixture only, and use of the new rear beam stop resulted in attainment of very low debris levels after a given ion diode shot on HERMES.

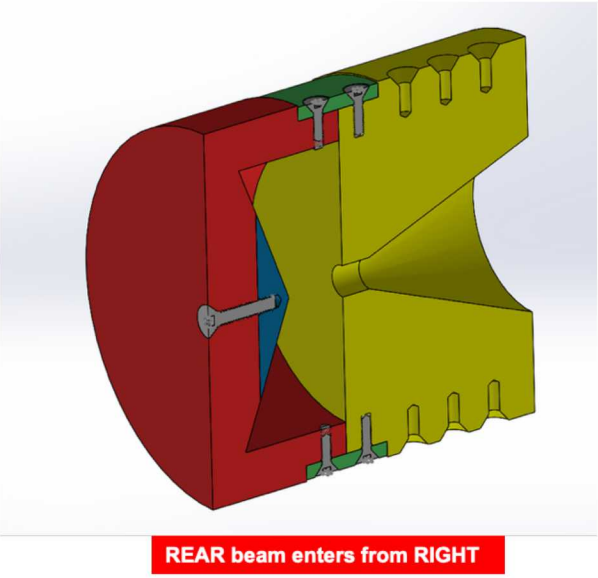

Fig. 21a

Fig. 21b

8. MCNP SIMULATIONS TO PREDICT NEUTRON FLUENCE AND SPECTRUM

The MCNP simulation code [7,8] is a general purpose Monte Carlo N-Particle Code that characterizes neutron, photon, electron, and coupled neutron/photon/electron transport. It can be used for, among other applications, radiation protection and dosimetry, and nuclear criticality safety. It has been extensively validated [33] in many Reports, Journal articles, and Conference presentations.

To make use of MCNP for this project for neutron characterization, the following steps are outlined:

1) Define locations of interest for neutron characterization. A top-view schematic drawing of the HERMES accelerator in the Bldg 970 high-bay is shown in Fig. 22. In the drawing, the HERMES test cell, where the ion beam source ("neutron source location") is located, is to the right. It is at this location where the neutron fluence and spectrum are predicted, as this is the location of test objects. On the left side of the drawing, in the high-bay, is the Control Console, the location at which the HERMES machine operators are located. Since the Console must be occupied during a machine shot, it is of interest to estimate any personnel exposure from neutrons (and photons) from a HERMES shot. In between these locations is the HERMES accelerator itself. The location

of hardware and fluids (water and transformer oil) must be carefully characterized, as these materials act to attenuate the neutron flux as it transits the machine.

2) Define the proton pulse (voltage, current, temporal duration, and spatial location) as input parameters for MCNP. These are estimated from the LSP modeling previously discussed. Run the simulation to obtain neutron tallies at the source location for estimates of total flux and spectrum.
3) Model the neutron propagation path through the HERMES hardware, and estimate total neutron dose at the Operations Console location. For this, a 3-dimensional model of HERMES hardware and fluid locations is used.

The results of the predicted neutron dose at the Operations Console will be discussed in the next section. In this section, total neutron production into 4π as well as predicted neutron fluence and spectrum at the test object location will be reviewed. Results will be compared for three different cases: 1) a thick-target as the neutron source, as referred to in Section 1. Tantalum is the target metal; 2) a dual-foil target, again as discussed in the first section, as a configuration that can yield higher neutron fluence than the thick-target; and 3) an evaluation of the neutron generation potential of the standard bremsstrahlung electron diode (photoneutrons). For this set of simulations, the measured voltage waveshape from ion diode shots will be used, as well as current shape taken from LSP simulations. The proton voltage will be assumed to have a peak of 13.5 MV, forward current is assumed to peak at 100 kA, and a rear proton beam current (co-moving with the high-energy electrons) is assumed to reach 50 kA peak.

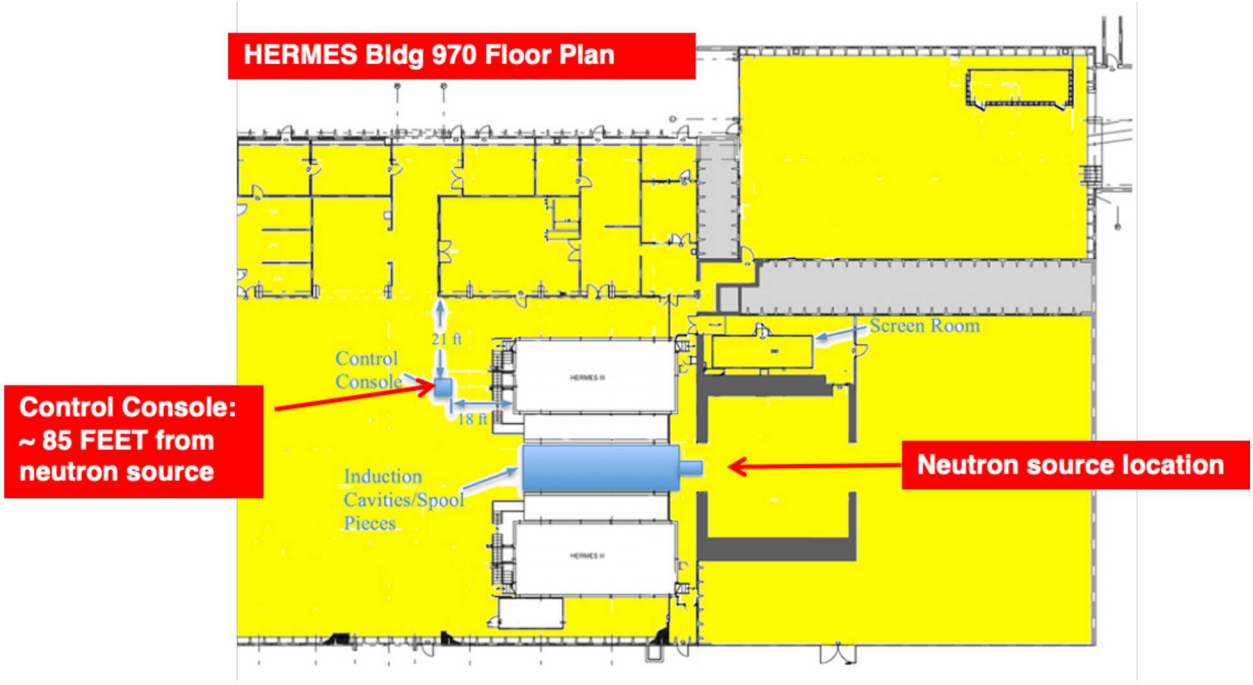

Fig. 22

The first results shown in Figs. 23 pertain to the total neutron production (into 4π) of the three neutron sources. Total neutron output (independent of energy) is compared for the three neutron sources in Fig. 23a. It can be seen that the HERMES photoneutron source is predicted to produce the highest total number of neutrons at ~ 2.7×10^{13} into 4π. The thick-target Ta yields significantly less at 9.3×10^{12}, whereas the double foil target (here cobalt plus niobium foils) yield lies in between at 1.7×10^{13}. The photoneutron estimate can be compared to the results of the earlier photoneutron experiments conducted by Sanford *et al* [5] in the early 1990s. In the earlier study, a total measured photoneutron output was

estimated "on the order of 10^{14} neutrons." The operational conditions for HERMES were different from present ones,

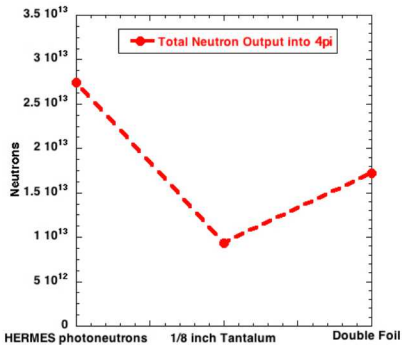

Fig. 23a

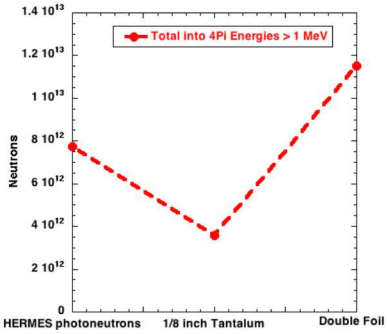

Fig. 23b

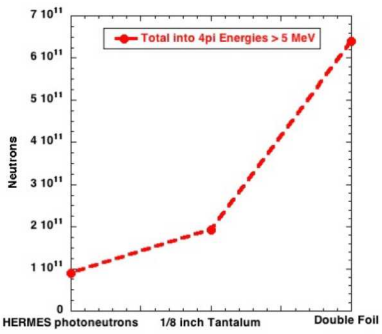

Fig. 23c

particularly the converter thickness and the level of Marx charge (higher), which lead to an estimate of 19 MV at the diode, instead of the more typical present estimate of 17-18 MV, caused mostly by a lower Marx charge. In addition, the neutron output from the uranium target fielded was twice that of the lead target, principally due to the additional photofission reactions in the uranium. Given these factors, the 2.7 x 10^{13} prediction is consistent with the measured results from the earlier work, lending credence to the present MCNP simulation accuracy.

When neutron energies are limited to those of a) greater than 1 MeV (Fig. 23b) and b) greater than 5 MeV, the relative yields of the three sources change significantly. For neutron energies > 1 MeV, while the thick-target Ta has still the lowest, the double-foil target neutron yield exceeds that of the photoneutron source by 50%. This is significant, since the neutron yield of both ion diode targets consists of 60% or more 1 MeV neutrons. When the neutron energy is restricted to > 5 MeV, the photoneutron source is by far the lowest, and the double-foil target by far the highest by a factor 7. While the percentage of 5 MeV neutrons from the double-foil target is small (~ 6%), it is the higher-energy neutrons that have the most effect on test samples.

We now switch from focusing on total neutron output to neutrons in the forward direction, since that is the presumed location of test samples located in the forward test fixture. A forward angle of 18° to 0° is chosen for comparison. A plot of total output into 18-0 for the three sources would look like the plot in Fig. 23 a, i.e. the photoneutron source would still produce the most total neutrons in the forward direction. The predicted *spectrum*, however, is quite different for the three cases. Predicted neutron spectra for the three cases is shown in Figs. 24, plotted in semi-log form (24a) and linear form (24b). The photoneutron spectrum is observed to reach maximum at relatively low neutron energy, < 2.5 MeV, where it exceeds both ion diode neutron targets in yield. Above 2.5 MeV, however, the spectrum declines steadily in yield to below 2e7 neutrons into the forward 18 – 0° cone at 10 MeV energy. Either ion diode target yields significantly more neutrons in energies above 5 MeV than the photoneutron yield. Compared to the thick-target Ta source, the dual-foil source yields many more neutrons at all energies 1 MeV, thus demonstrating the (predicted) yield superiority of the dual-foil target.

In the earlier work published by Sanford et al [5], there is shown (Fig. 11 in the paper) a measured photoneutron spectrum from HERMES Shot 2000. We compare the measured spectrum from a HERMES shot taken in the early 1990s with the MCNP-predicted spectra plotted in Figs. 24. The added spectral data from the earlier shot is shown (BLACK) in Fig. 25. As stated before, there are aspects of HERMES bremsstrahlung performance that have changed since the early 1990s (lower Marx charge, different converter thickness), but the added data taken from dosimetry measurements provides a useful

comparison with more recent MCNP simulation data. In Fig. 25, it can be seen that the MCNP photoneutron prediction significantly exceeds the measured data for energies < 3 MeV, but the spectral shape follows an almost identical drop-off for neutron energies above 4 MeV. This gives added confidence that the MCNP modeling of the HERMES photoneutron spectrum is reasonably accurate.

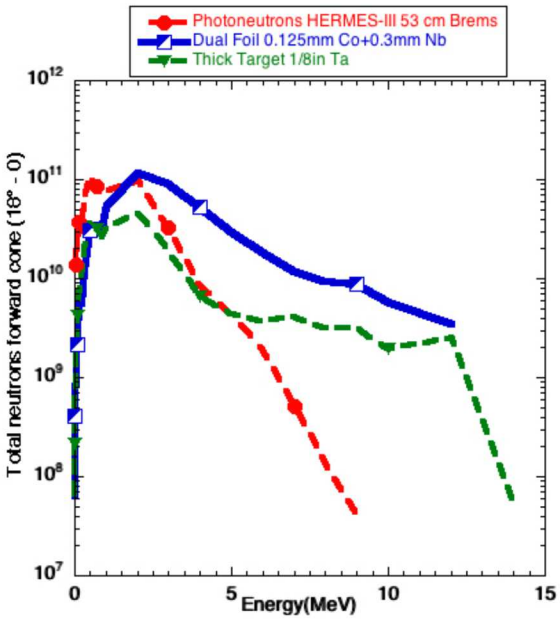

Fig. 24a

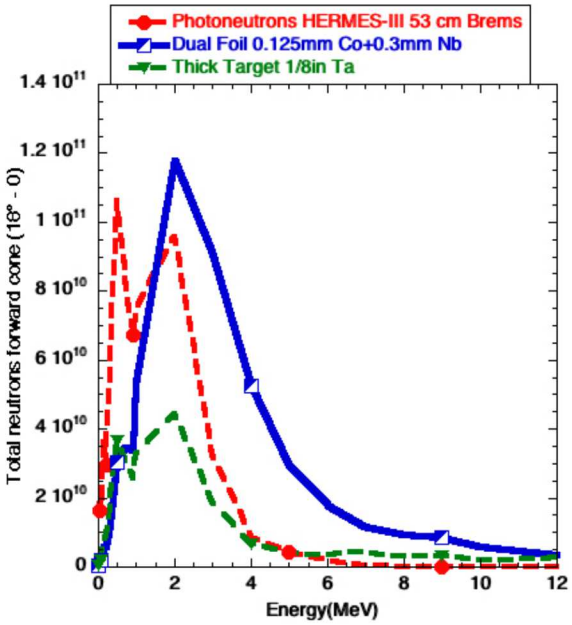

Fig. 24b

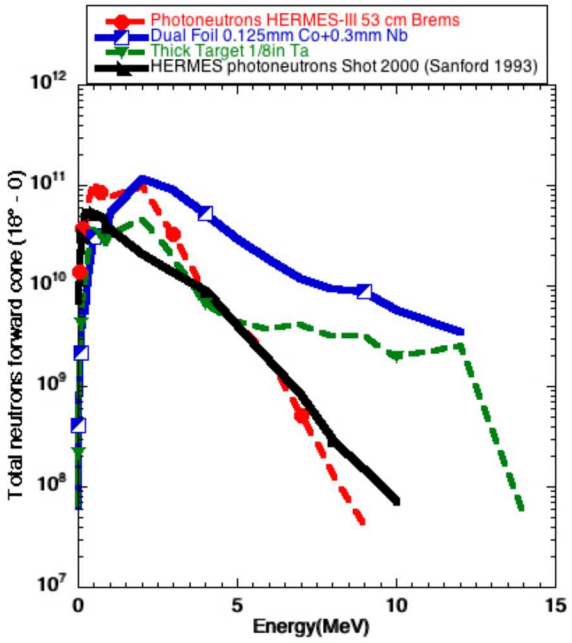

Fig. 25

The predicted neutron spectrum from ion diode can also be compared to two well-known neutron sources, using MCNP predictions for those sources. One is the Annular Core Research Reactor (ACRR), located at Sandia, and the other is a Cf252, a radioactive element and a standard source of high-energy neutrons. For the comparison, the double-foil neutron target plotted in Figs. 24 and 25 is used. For the comparisons, the spectra are normalized to unity, since the specific outputs are very different between the sources.

The first comparison is between ion diode and ACRR. A plot of neutron spectra out to 15 MeV energy is shown in Fig. 26a. A separate plot emphasizing the energy range to 0.3 MeV is also shown, in Fig. 26b. It is observed that above ~ 0.3 MeV energy, there are relatively many more high-energy neutrons in the ion diode spectrum compared to the ACRR spectrum. The closeup to 0.3 MeV plot (Fig 26b) is added to illustrate that the ACRR spectrum contains orders of magnitude more neutrons of very low energy than the ion diode spectrum, as can be expected from a fission source.

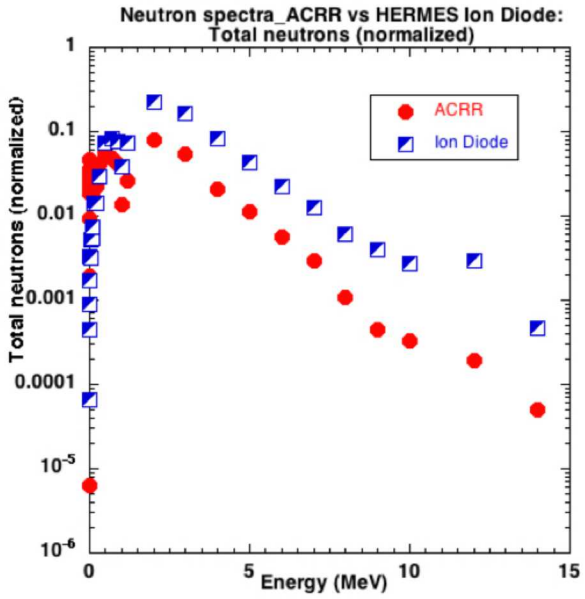

Fig. 26a

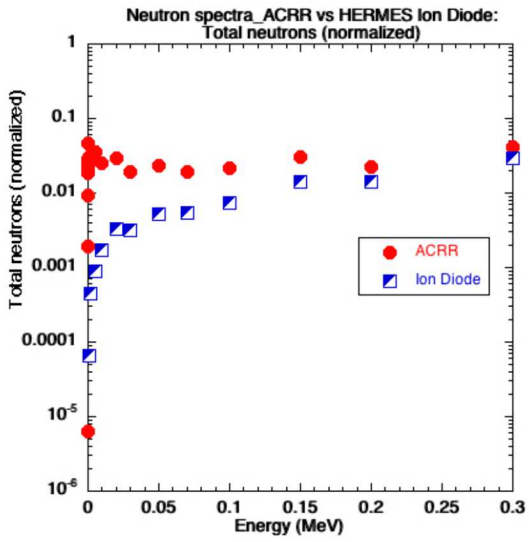

Fig. 26b

An analogous plot to Fig. 26a, but with a normalized Cf252 spectrum replacing the ACRR spectrum, is shown in Fig. 27a. Compared to the ACRR spectrum, that of the Cf252 is seen to be almost identical to the ion diode spectrum. The main difference occurs in the energy range < 0.2 MeV. As shown in Fig. 27b. In this range, the ion diode spectral values exceed those of Cf252, the opposite of the ACRR case.

8.1 **MCNP predictions of neutron flux uniformity in the Test Fixture.**

The interior volume of the forward test fixture (Fig. 18) is relatively large. The geometry is that of an upright cylinder of axial length 15 cm and diameter 20.3 cm. The specific fluence (in neutrons/cm^2) will vary significantly across this volume, being the highest for locations just behind the front fixture cover, and dropping more than an order of magnitude at the back of the cylinder opposite the front plate. The principal reason for this is that the neutron flux generated by (p,*x*n) events at the neutron foil location is

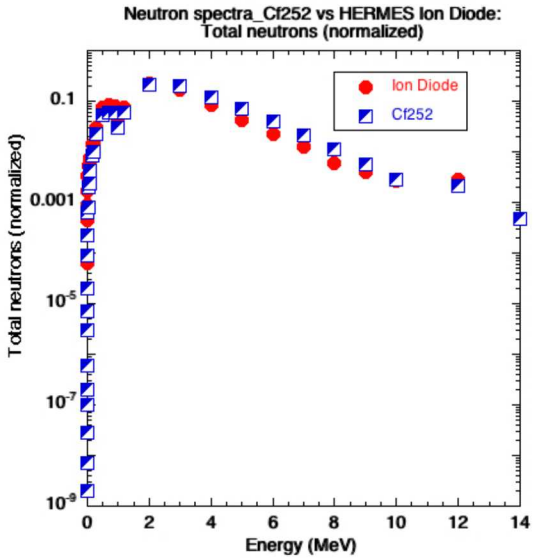

Fig. 27a

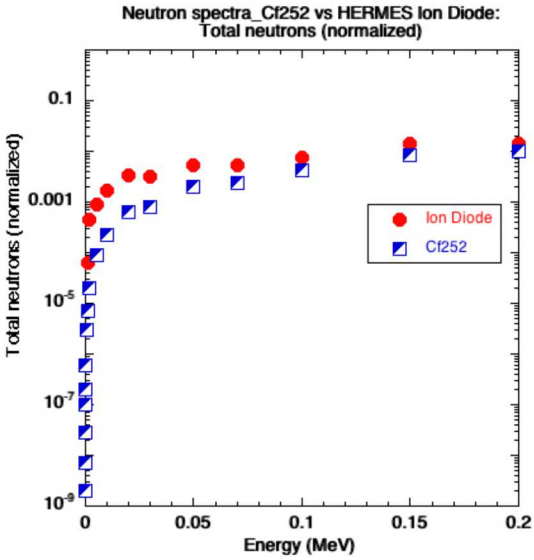

Fig. 27b

largely (but not completely) azimuthally symmetric, and so fluence levels are maximized at positions closest to the neutron source. To assess uniformity of neutron output, the fixture plate was divided into 11 radial segments of 1 cm radial width. The MCNP results were then tallied at a z-location just behind the fixture plate, i.e. as close to the neutron source as possible within the test fixture volume. The geometry of the tally is shown in Fig. 28a, and fluence (in neutrons/cm^2) is shown as a function of ring number in Fig. 28b, for three different energy cuts: a) all neutrons, b) neutrons energies > 1 MeV), and c) neutron energies > 5 MeV. Neutron dose uniformity is seen to be about the same for any of the energy cuts, being relatively constant to edge of ring number 3. Peak neutron flux is predicted to be about 1.8 x 10^{11} neutrons/cm^2, and fall to 1.6 x 10^{11} at ± 3 cm from the fixture axis. Total dose falls to almost zero at ± 6 cm from the axis. Contributions from the rear neutron foil (before it was removed) were tallied at the same location as in Figs. 28, and found to be insignificant. This is due to the distance of the rear neutron source from locations behind the front plate. It is emphasized here that the relative non-uniformity of the neutron dose across the front plate, and the lack of contribution from any rear neutron target, is not due to neutron attenuation, but due to the combination of a relatively small neutron target radius (4.6 cm) and almost complete azimuthal symmetry of the neutron output.

9. DOSIMETRY MEASUREMENTS COMPARED TO MCNP PREDICTIONS

After the initial set of 55 dosimetry and device sample was inadvertently exposed to possible proton impingement due to penetration of both test fixtures, only 4 additional nickel foils were exposed to further shots. In the additional experiments, a single foil was placed just behind the front fixture plate, the same location as the tallies from MCNP simulations discussed with Figs. 28. Another foil was placed at the back of the fixture volume near the cylinder axis. Both front foils were exposed on more than one ion diode shot. Dosimetry results on the foils were hard to analyze, because the relative counts were small, certainly much smaller than samples from the ACRR facility. The rear-located foils gave no discernible reading [34], and the front samples, as well as a few foils from the initial batch of 55 samples, were

Fig. 28a

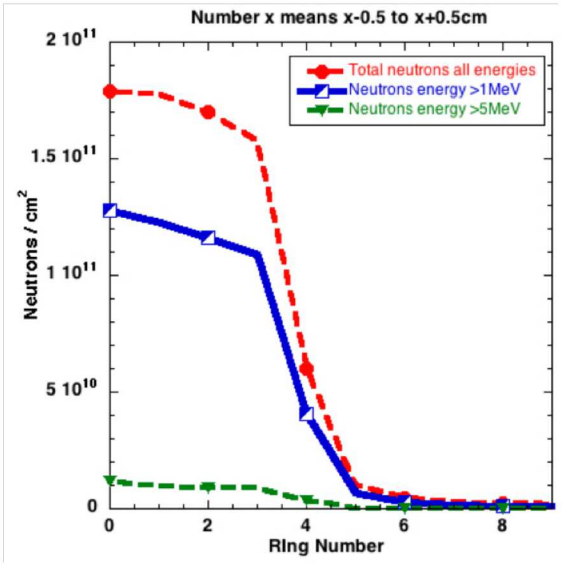

Fig. 28b

estimated to read between 1 x 10^{10} and 1 x 10^{11} neutrons/cm^2 [35]. The upper value is consistent with MCNP simulation predictions. In addition, evidence from two Si photodiodes exposed as part of the 55 initial samples were found to have leakage current degradation that is at least partially ascribable to displacement (i.e. neutron) damage [36]. Clearly, these results are incomplete, and more experiments need to be undertaken with more and varied dosimetry samples to obtain better estimates of neutron fluence and uniformity at the front test fixture location.

There is another source of experimental verification with the MCNP results. For the ion diode shots (and additional bremsstrahlung shots), a device known as the "Albatross" was fielded by Radiation Protection Staff, directed by Alexandra Robinson (Org. 625). The device, originally developed starting the 1970s by Los Alamos National Laboratory (LANL), is manufactured by Health Physics Instruments (HPI) in Goleta, Ca, and is sold commercially as Model 2080B Pulse Neutron Survey Meter. Documentation is available from both HPI and LANL [16,17]. A short description of Albatross operation is here provided by Alexandra Robinson:

The instrument uses the principal of nuclear capture to detect the neutrons. A 25 cm diameter polyethylene pseudosphere moderator thermalizes the neutrons. They are then captured by silver foil. The resulting beta activity is proportional to the previously acquired neutron dose. The betas are detected by a GM tube that is wrapped with the silver foil. Since the GM tube is also sensitive to external radiation not from the silver foil, a second GM tube is used to cancel out any background gamma radiation. The second GM tube is covered with tin. This presents the same gamma attenuation as the silver.

The counts from each detector are scaled in two separate scalers. The response from the two detectors may not be the same to gamma rays due to differences in detector volume, gas pressure or shielding. The count rate from the two tubes must be matched within 1%. The software multiplies the counts from each scaler to balance them, and then subtracts the gamma counts from the neutron counts to obtain Net Neutron counts. It then divides this number by a calibration factor to obtain a corrected reading. The resulting values, because of the low counting rate, need to be averaged over a period of time. This is performed by the digital filter. In essence, it is a 16 register rotating stack that stores each new value over

the oldest one. The time taken for a sample is determined by the average time. The alphanumeric display can display several different parameters and functions besides the radiation level. In addition, the microprocessor controls the outputs, lights, relay, and horn.

The Albatross is an instrument that provides us an ability to accurately detect neutron dose (tissue equivalent) independent of precise neutron energy spectrum knowledge in real time based on the principal of nuclear capture to detect neutrons in the field. Neutrons from pulsed or steady-state neutron sources activate an internal silver foil, for which the resultant betas produced are measured with an internal GM counter. A second internal GM counter is used to subtract any gamma background present during the count. This activation method allows for use in very quick pulsed neutron fields for which active measurement is typically not possible. This instrument is maintained/calibrated by the manufacturer with traceability to NIST, with a verified instrument response against PuBe sources at RPI within 11% of the expected dose rate.

For the measurements described here, the Albatross is fielded inside a copper screen box and placed at the Operations Console location (see Fig. 22). An additional Albatross was fielded inside the experimenter's screenroom, but will not be discussed here. It is mentioned here that while Albatross data are valuable for cross-comparisons such as described here, they have not been certified for use for surveys of record. That assessment instrument is known as 9/3-Inch Spheres. Such spheres have been fielded on both ion diode and bremsstrahlung shots, but to date have not provided a useful dataset for analysis, apparently due to insufficient fluence levels from both kind of shots for the instrument.

This leaves the Albatross data that can be compared to MCNP simulation predictions. For the simulations already discussed above, the assumed peak proton energy and peak proton current were assumed to be 13.5 MeV and 100 kA, respectively. Under these assumptions, the MCNP-predicted neutron dose at the Operations Console is 0.025 mrem/shot. This can be compared to 4 Albatross post-shot readings taken at different times during the Project: 0.127, 0.170, 0.162, and 0.199 mrem. The last number was recorded after the last shot taken during the Project, in September 2019, and represents a factor 8 increase over the MCNP prediction. To try and reconcile the increase with the MCNP prediction, subsequent simulations were performed, in which two changes were made to the proton energy and current assumptions: 1) peak voltage was raised from 13.5 MeV to 16 MeV, with peak current kept constant. This raised the predicted dose at the Console from 0.025 to 0.100 mrem; peak voltage was kept at the higher 16 MeV value, and peak proton current was raised to 200 kA. The resultant MCNP prediction was 0.170 mrem. While still below the highest recorded Albatross value, this exercise indicates that MCNP can be aligned more closely with the Albatross readings by what may be termed as reasonable increases in both proton energy and current. The increase in assume proton energy is reasonable because in the LSP simulations, the bound current at z = - 2meters consistently showed a retrapping wave that was higher than those recorded on HERMES shots. A lower value of retrapping wave indicates coupling to a higher diode impedance, which is in the right direction to match the 16 MeV proton energy needed to help close the gap between MCNP and Albatross readings. An assumed 200 kA of proton current raises the ion efficiency estimate to ~ 28%, higher than that initially assumed by this Project (20%), the lower number which was consistent with earlier ion diode experiments at other facilities at high diode impedance. But all the previous ion diode experiments were obtained using the axial diode geometry, and indeed, the radial geometry used in this Project is the first known use of the radial ion diode for a non-power-converging geometry. A higher attained ion efficiency would thus not be out of line with previous efficiency estimates.

It must be pointed out that if both the proton energy and current assumptions are raised to match the Albatross data at the console, then the proton fluence and uniformity estimates (Figs. 24 – 28) should be raised as well, and this would result in less consistency with the dose estimates from the nickel foils. This further emphasizes the conclusion that more dosimetry measurements need to be made in order to obtain more accurate estimates of proton fluence in neutrons/cm^2 at the location of test objects.

There is one further data point of comparison of MCNP predictions with Albatross results. MCNP simulations performed with the bremsstrahlung diode geometry predict a neutron dose reading at the Console of 0.020 to 0.050 mrem. The Albatross has been fielded on a significant number of HERMES bremsstrahlung shots, and a survey of the results yields an average of 0.050 mrem/shot. This value is thus consistent with the MCNP predictions for this geometry, and gives further evidence that the MCNP simulations give an accurate prediction of neutron dose at the Operations Console, and thus help to validate the assumptions of proton energy and current that were used.

10. CONCLUSIONS AND SUGGESTIONS FOR FUTURE WORK

The conclusion in this section largely repeat those listed in the Executive Summary above. The HERMES ion diode neutron source LDRD appears to have achieved its key goal of ~ few $x10^{10}$ pulsed neutrons/cm^2 at a test object location. Further neutron measurements are needed to confirm this. The HERMES radial ion diode operation, previously developed at half-power (6 MeV), was successfully extended to an estimated 16 MeV (peak) and 200 kA proton current, thus making this ion beam the most powerful known in the world. At Sandia, such energetic ions have not been produced since the PFBA-II experiments [10,11]. MCNP and LSP simulations were key to understanding diode performance and predicting neutron output and spectrum. Despite this power, the contents of the test fixture, located as close as 1.25 cm to the neutron source, are undamaged after multiple ion beam pulses. Results show that beam/target interaction, used on a > 10 MeV platform, can yield a pulsed neutron flux that is competitive with photoneutrons and dense plasma focus (DPF) as a neutron source. The radial ion diode is operationally successful, being operated with minimal debris and activation, and could be inserted readily into the normal bremsstrahlung operation, thus minimally impacting the HERMES main validation mission.

For this source to be useful for applications, the neutron spectrum and fluence must be better defined, and measured at a number of positions in the test fixture. This would require more extensive fielding of dosimetry foils. It would also be worthwhile to determine more accurately the level of proton current and diode voltage than was achieved for this Project. This latter goal is rendered challenging, simply because of the power of the incoming ion beam to damage beam diagnostics placed in its path, and the limited volume for diagnostic placement (i.e. inside the HERMES center conductor). Such follow-on work, however challenging, may be judged as worthwhile, considering the considerable potential that is already shown for this type of neutron source.

REFERENCES

1. J.D. Lindl et al., *The physics basis for ignition using indirect-drive targets on the National Ignition Facility*, Phys. Plasmas 11, 339 (2004).

2. OMEGA Laser – Laboratory for Laser Energetics, http://www.lle.rochester.edu/omega_facility/omega/

3. M. Krishnan, *The Dense Plasma Focus: A Versatile Dense Pinch for Diverse Applications*, IEEE Trans. Plas. Sci **40**, 3189 (2012).

4. M. J. Berger and S. M. Seltzer, *Bremsstrahlung and Photoneutrons from Thick Tungsten and Tantalum Targets*, Phys. Rev. C **2**, 621 (1970).

5. T. W. L. Sanford, L. J. Lorence, J. A. Halbleib, J. G. Kelly, P. J. Griffin, J. W. Poukey, W. H. McAtee & R. C. Mock, *Photoneutron Production Using Bremsstrahlung from the 14-TW Pulsed-Power HERMES III Electron Accelerator*, Nucl. Sci. Engin. **114**, 190 (1993).

6. N. Soppera, E. Dupont, M. Bossant, *Janis Book of proton-induced cross-sections*, OECD NEA Data Bank, June 2012.

7. MCNP (https://mcnp.lanl.gov) and Monte Carlo N-Particle are registered trademarks owned by Triad National Security, LLC, manager and operator of Los Alamos National Laboratory.

8. J. F. Briesmeister, *MCNP – A general Monte Carlo N-particle transport code, Version 4C*, Los Alamos National Laboratory, Los Alamos, NM, LA-13709-M, Mar. 2000 (unpublished).

9. D. J. Johnson, R. J. Leeper, W. A. Stygar, R. S. Coats, T. A. Mehlhorn, J. P. Quintenz, S. A. Slutz and M. A. Sweeney, *Time-resolved proton focus of a high-power ion diode*, J. Appl. Phys **58**, 12 (1985).

10. D. J. Johnson, S. E. Rosenthal, R. S. Coats, M. P. Desjarlais, T. R. Lockner, T. A. Mehlhorn, T. D. Pointon, C. L. Ruiz, W. A. Stygar, S. A. Slutz, and D. F. Wenger, *Lithium beam generation and focusing with a radial diode on PNFA-II*, Laser Part. Beams 16, 185 (1998).

11. T. J. Renk, G. C. Tisone, R. G. Adams, D. J. Johnson, and C. L. Ruiz, *Development of the laser evaporation ion source for lithium beam generation on the Particle Beam Fusion Accelerator (PBFA-II)*, Phys. Plasmas 6, 3697 (1999).

12. T. J. Renk, P. P. Provencio, S. V. Prasad, A. S. Shlapakovski, A. V. Petrov, K. Yatsui, W. Jiang, and H. Suematsu, *Materials Modification Using Intense Ion Beams*, Proc. Of the IEEE **92**, 1057 (2004).

13. Timothy J. Renk, Victor Harper-Slaboszewicz, Kenneth A. Mikkelson, W. Craig Ginn, Michael Schall and Gary Cooper, *Use of radial self-field geometry for intense pulsed ion generation above 6 MeV on Hermes III*, Sandia Report SAND2012 – 10744, Printed December 2012.

14. T. J. Renk, Victor Harper-Slaboszewicz, K. A. Mikkelson, W. C. Ginn, P. F. Ottinger, and J. W. Schumer, *Use of a radial self-field diode geometry for intense pulsed ion beam generation at 6 MeV on Hermes III,* Phys. Plasmas **21** (2014), 123114-1 - 123114-17.

15. D. R. Welch, D. V. Rose, M. E. Cuneo, R. B. Campbell, and T. A. Mehlhorn, *Integrated simulation of the generation and transport of proton beams from laser-target interaction*, Phys. Plasmas **13**, 063105 (2006).

16. Health Instruments Physics, *Operations and Repair Manual, Model 280B Pulse Neutron Survey Meter*, August 2015. Available from Health Physics Instruments. 330 D South Kellogg Ave, Goleta, CA. Tel 1-805-967-8422.

17. A. L. Justus et al, *Recent Firmware and Hardware Upgrades to the HPI2080 Pulsed Neutron REM Meter*. Email: tmclean@lanl.gov

18. The SRIM code can be obtained from www.srim.org.

19. A. Mohammadi, S. Hamidi, Mohsen Asadi Asadabad, *The use of the SRIM code for calculation of radiation damage induced by neutrons*, Nucl. Instr. Meth. Phys. B **412**, 19 (2017).

20. S. J. Stephanakis, D. Mosher, G. Cooperstein, J. R. Boller, J. Golden, S. A. Goldstein, *Production of Intense Proton Beams in Pinched-Electron-Beam Diodes*, Phys. Rev. Lett. **37**, 1543 (1976).

21. S.A. Goldstein, G. Cooperstein, R. Lee, D. Mosher and S.J. Stephanakis, *Focusing of Intense Ion Beams from Pinched-Beam Diodes*, Phys. Rev. Lett. **40**, 1504 (1978).

22. S. E. Rosenthal, *Characterization of electron flow in negative- and positive-polarity linear induction accelerators*, IEEE Trans. Plasma Sci. **19**, 822 (1991).

23. C.W. Mendel, D.B. Seidel, and S.A. Slutz, Phys. Fluids **26**, 3628 (1983).

24. C.W. Mendel, D.B. Seidel, and S.E. Rosenthal, Laser Part. Beams **1**, 311 (1983).

25. P.F. Ottinger and J.W. Schumer, Phys. Plasmas **13**, 063109 (2006).

26. P. F. Ottinger, T. J. Renk, and J. W. Schumer, Phys. Plasmas **26** 023105 (2019).

27. F. C. Young et al, Bull. APS **37**, 1562 (1992).

28. E. Rutherford, *The Scattering of α and β Particles by Matter and the Structure of the Atom*, Philosophical Magazine **6** (21), 669 (1911).

29. F. C. Young, J. Golden, and C. A. Kapetanakos, *Diagnostics for intense pulsed ion beams*, Rev. Sci. Instr. **48**, 432 (1977).

30. M. O. Thompson and T. J. Renk*, Numerical modeling and experimental measurements of pulsed ion beam surface treatment*, Mat. Res. Soc. Symp. Proc. **504**, 33 (1998).

31. Michael E. Cuneo (1650), private conversation.

32. S. I. Stoliarov, Richard N. Walters, *Determination of the heats of gasification of polymers using differential scanning calorimetry*, Polymer Degradation and Stability 93, **422** (2008).

33. Russell D. Mosteller, Bibliography of MCNP Verification and Validation: 1990 – 2003, Los Alamos National Laboratory **LA-UR-03-9032** (unpublished).

34. Thomas J. Quirk (1386), private conversation.

35. Thomas J. Quirk and William J. Martin (1384), private conversations.

36. Brandon A. Aguirre (1384), private conversation.

DISTRIBUTION

2 Dr. Paul F. Ottinger
2700 E. Cherry Creek South Drive Unit 317
Denver, CA 80209

2 Dr. Bruce V. Weber
Code 6773
Naval Research Laboratory
4555 Overlook Ave, SW
Washington, DC 20375

2 Russell Durrer
56 Fox Place
Pagosa Springs, CO 81147

1	MS1106	Andrew Biller	Org. 1342
1	MS1106	Sean K. Coffey	Org. 1342
1	MS1106	Benjamin M. Hughes	Org. 1342
1	MS1106	Nathan R. Joseph	Org. 1342
2	MS1106	Debra S. Kirschner	Org. 1342
1	MS1106	John A. Lott	Org. 1342
1	MS1106	Israel Owens	Org. 1342
1	MS1141	Theodore C. Grabowski	Org. 1385
1	MS1142	Tom Quirk	Org. 1386
1	MS1146	William Martin	Org. 1384
1	MS1146	Brandon Aguirre	Org. 1384
1	MS1153	David Gardner	Org. 5498
4	MS1167	Bryan V. Oliver	Org. 1340
1	MS1169	Patrick Griffin	Org. 1000
1	MS1182	Jason Shelton	Org. 5499
5	MS1182	Timothy Renk	Org. 5499
1	MS1190	Timothy Webb	Org. 1676
1	MS1195	Michael Cuneo	Org. 1650
1	MS1195	Mark Kiefer	Org. 1651
1	MS1195	Michael Mazarakis	Org. 1656
1	MS1196	Mark Johnston	Org. 1659
1	MS1196	George Laity	Org. 1659

1	MS0899	Technical Library	9536 (electronic copy)

Sandia National Laboratories